



Development and Evaluation of Reduced Kinetics Models for 1,3-Butadiene–Air Combustion

Ryan DeBoskey*

NC State University, Raleigh, North Carolina 27695

David A. Kessler,[†] Brian Bojko,[†] Ryan F. Johnson,[‡] Andrew Kercher,[‡] and Eric Ching[‡]

Naval Research Laboratory, Washington, District of Columbia 20170

and

Venkateswaran Narayanaswamy[§]

NC State University, Raleigh, North Carolina 27695

<https://doi.org/10.2514/1.B39768>

The present work details the development and evaluation of two-step and six-step finite-rate chemistry mechanisms for 1,3-butadiene oxidation in air, relevant for hypersonic airbreathing engines utilizing hydroxyl-terminated polybutadiene (HTPB). A sensitivity study was performed to calibrate the pre-exponential factor of the Arrhenius rate expressions for reproducing laminar counterflow-diffusion flame behavior and extinction strain rate. Evaluation of the calibrated mechanisms was performed for a model one-dimensional solid-fuel counterflow diffusion flame and two-dimensional axisymmetric large-eddy simulation of a solid-fuel ramjet combustor. A 20-species pressure comprehensive skeletal mechanism serves as a baseline for model evaluation. The simulations utilized interfacial solid–gas coupling to evaluate the influence of the reduced mechanisms on the regression rate of solid fuel and coupled flame dynamics. The results established that both two-step and six-step mechanisms are capable of predicting salient features of HTPB–air combustion, with the six-step mechanism providing superior accuracy in the prediction of flame temperatures, species mass fractions, and regression rates in time-resolved solid-fuel ramjet simulations. Although the reduced mechanisms have limited utility when it comes to capturing all relevant turbulence and chemistry interactions due to the lack of available chemical pathways, both reduced mechanisms showed significant computational speedup in comparison to the skeletal mechanism.

Nomenclature

A	= cross-sectional area, m ²
a	= strain rate, 1/s
c^*	= characteristic velocity, m/s
d	= diameter, m
h	= backward-step height, m
L	= length, m
MSE	= mean-squared error
\dot{m}	= mass flow rate, kg/s
P	= pressure, atm, kPa
r	= radius, m
\dot{r}	= regression rate, m/s
S	= sensitivity coefficient
T	= temperature, K
x	= axial length, m
Y	= mass fraction
ℓ	= flame thickness, mm
Δh	= grid spacing, μm
Δt	= time step, s

ζ_θ	= azimuthal vorticity, 1/s
ρ	= density, kg/m ³
τ	= ignition delay, s
ϕ	= equivalence ratio
Ψ	= flame edge

Subscripts

p	= port
in	= inlet
t	= stagnation, throat

I. Introduction

H YDROXYL-TERMINATED polybutadiene (HTPB) has long been utilized and studied as a propellant binder in solid-rocket motors [1,2]. HTPB is a high-density polymer, traditionally serving as both a fuel and a binder for oxidizer components, commonly ammonium perchlorate (AP), and energetic fuels, including solid particles. Recently, HTPB has gained interest in its role as the primary fuel in hybrid rocket engines (HREs) and solid-fuel ramjet (SFRJ) engines [3,4]. In contrast to traditional solid-rocket motors, oxidizer is supplied externally from the combustion chamber in the form of ingested ambient air, eliminating the need for the solid propellant to contain oxidizing components. As a result, SFRJ engines offer unique propulsive benefits, including extended range and specific thrust [5]; however, the scalability and current deployment of SFRJs are severely limited due to the lack of physical understanding and control of the complex combustion dynamics across a range of flight operating conditions. Numerical simulation offers a promising means to investigate the multiphysics combustion characterized by coupling between gas-phase chemical kinetics, phase change and decomposition of solid fuel, turbulent mixing, and heat and mass exchange at the fluid–solid interface. However, due to very high Reynolds numbers in SFRJs and the need for multiphysics modeling, detailed finite-rate chemical kinetics are prohibitively expensive, requiring the use of reduced-order models

Received 30 August 2024; accepted for publication 10 February 2025; published online 28 April 2025. This material is declared a work of the U.S. Government and is not subject to copyright protection in the United States. All requests for copying and permission to reprint should be submitted to CCC at www.copyright.com; employ the eISSN 1533-3876 to initiate your request. See also AIAA Rights and Permissions <https://aiaa.org/publications-publish-with-aiaa/rights-and-permissions/>.

*Ph.D. Student, National Defense Science and Engineering Graduate Fellow, Department of Mechanical and Aerospace Engineering; also Commonwealth Technology Innovation LLC, A Huntington Ingalls Industries Company; rddebosk@ncsu.edu. Student Member AIAA (Corresponding Author).

[†]Director, Laboratory for Computational Physics, Senior Member AIAA.

[‡]Research Scientist, Laboratory for Computational Physics, Member AIAA.

[§]Professor, Department of Mechanical and Aerospace Engineering, Associate Fellow AIAA.

for time-resolved numerical simulations at typical operating conditions for full-scale SFRJ engines [6–8]. Therefore, the development of reliable reduced-order models is critical to the development of the future of SFRJ technology.

The chemical decomposition of HTPB is a complicated coupling process between the gas-phase kinetics of heat release and the solid-fuel pyrolysis. The combustion of solid fuels is largely restricted to the gas-phase combustion of the pyrolysis products above the fuel grain surface [2], with HTPB in hybrid rocket configurations found to have little to no melt layer [9]. Typically reduced-order modeling approaches neglect the liquid multiphase layers seen in HTPB decomposition [8,10,11]. Notably, recent synchrotron-based phase-contrast imaging of the HTPB solid-fuel surface has shown the local presence of small molten liquid and bubbling layers in small-scale SFRJs [12]. Empirical evidence indicates that 1,3-butadiene, C_4H_6 , is the major gaseous decomposition species of HTPB. Early work by Arisawa and Brill utilizing flash pyrolysis demonstrated that the major decomposition species of HTPB were trans-butadiene oligomers, contrary to previously held belief [13]. This work was expounded upon by Chiaverini et al., who performed mass spectrometry on the decomposition pyrolysis products of HTPB [14], finding 1,3-butadiene to be the main pyrolysis product across a range of pyrolysis surface temperatures. Recently, Bojko et al. [15] and Gross et al. [16] investigated the major species and near-wall flame dynamics of composite AP/HTPB propellants, assuming 1,3-butadiene to be a major decomposition species of HTPB, with successful comparison to burn-rate experiments. Furthermore, pyrolysis mass spectrometry of AP/HTPB composites showed that decreased AP mass fraction resulted in increased amounts of 1,3-butadiene in the pyrolysis products [17].

Influenced by the experimental body of work, reduced-order modeling of the HTPB decomposition typically assumes that 1,3-butadiene is the main and only pyrolysis product [8,10,11]. Therefore, capturing the combustion dynamics of pure HTPB led to the development of detailed gas-phase kinetics mechanisms for 1,3-butadiene combustion [18,19]. Additionally, due to its role as an intermediate in soot production, 1,3-butadiene has been included in several other detailed kinetics mechanisms [20,21]. However, due to the inclusion of hundreds of species and thousands of reactions, these detailed mechanisms are largely restricted to zero- and one-dimensional problems.

Development of reduced-order HTPB/oxygen models has been paramount to enabling high-fidelity numerical simulations of HREs. Sankaran et al. developed a global two-step reaction mechanism based on the work of Westbrook and Jones for the combustion of HTPB in hybrid rocket engines that assumes 1,3-butadiene to be the main product of HTPB pyrolysis [22]. This model has been adapted and extensively used for numerical simulations, but the simplified global mechanism consistently overpredicts flame temperature. To circumvent this problem, Frassoldati et al. included radical recombination reactions to mitigate flame temperature and proposed a six-step reaction mechanism, based on the work of Jones and Lindstedt, for hybrid rocket HTPB combustion [23]. Giarani et al. [24] utilized the two-step and six-step reaction mechanisms to perform parametric Reynolds-averaged Navier-Stokes (RANS) simulations of a hybrid rocket motor. Subsequently, Moringo et al. [25] performed parametric LES simulations of the same geometry hybrid rocket motor to compare the various reduced 1,3-butadiene kinetics mechanisms. These RANS and LES simulations of hybrid rocket engines consistently showed overprediction of temperature with the two-step mechanism and found better agreement with experimental results using the six-step mechanism with included radical recomposition. Successful RANS and LES simulations have been conducted on high-density polyethylene (HDPE) SFRJ engines using reduced-order kinetics models [7,26] and alternative chemistry formulations [6], respectively. However, LES or RANS simulations of HTPB SFRJ engines are largely nonexistent in the literature [8,11,27] due to a lack of robust reduced-order kinetics models for 1,3-butadiene combustion with air.

Global combustion mechanisms offer the benefits of low cost and medium physical fidelity over a wide range of operating temperatures and pressures. The development of global reaction schemes has remained relatively unchanged for half a century. The seminal work by Westbrook and Dryer [28] outlines a global two-step/six-species reaction scheme that maintains pressure dependency and allows for calibration with experimental data across a range of equivalence ratios. The Arrhenius model parameters are modified in order to ensure accurate reproduction of empirical flame trends. The two-step global reaction is inexpensive but suffers from the overprediction of peak temperature and flame speeds, especially in high-temperature regimes. Further work by Jones and Lindstedt addresses this problem with the extension to a global 6-step/10-species reaction scheme that includes radical recombination reactions [29].

This work addresses this knowledge gap and delivers robust 1,3-butadiene kinetic mechanisms for efficient numerical simulations of HTPB-air combustion within SFRJ engines. First, the numerical methodology is described, and reduced-order kinetics models for 1,3-butadiene are introduced with reaction rates taken from literature. A baseline 109-step/20-species skeletal mechanism is introduced and validated against a 613-step/92-species detailed kinetics mechanism. A methodology for model calibration is outlined, and a sensitivity study is performed. To evaluate the performance of the reduced-order mechanisms, simulations are performed on model 1D solid-fuel counterflow and 2D axisymmetric solid-fuel ramjet test cases. Results are presented for each of the test cases, and conclusions are drawn regarding the applicability and limitations of the reduced-order kinetic models in the combustion of HTPB for SFRJ engines.

II. Numerical Method

A. Governing Equations

Inside the fluid domain, we solve the compressible, multi-component, chemically reacting Navier-Stokes equations, given generally by

$$\frac{\partial \mathbf{y}}{\partial t} + \nabla \cdot \mathcal{F}(\mathbf{y}, \nabla \mathbf{y}) - \mathcal{S}(\mathbf{y}) = 0 \quad (1)$$

where \mathbf{y} is the state vector, $\nabla \mathbf{y}$ is its spatial gradient, t is time, \mathcal{F} is the flux, and $\mathcal{S} = (0, \dots, 0, 0, \omega_1, \dots, \omega_{n_s})^T$ is the chemical source term, with ω_i corresponding to the net chemical production rate of the i th species. The physical coordinates are denoted by $x = (x_1, \dots, x_d)$, with d spatial dimensions. The vector of state variables is expanded as

$$\mathbf{y} = (\rho v_1, \dots, \rho v_d, \rho e_t, C_1, \dots, C_{n_s})^T \quad (2)$$

where ρ is density, $v = (v_1, \dots, v_d)$ is the velocity vector, e_t is the specific total energy, $C = (C_1, \dots, C_{n_s})$ is the vector of molar concentrations, and n_s is the number of species. The partial density of the i th species is defined as

$$\rho_i = W_i C_i \quad (3)$$

where W_i is the molecular weight of the i th species, from which the density can be computed as

$$\rho = \sum_{i=1}^{n_s} \rho_i \quad (4)$$

The mole and mass fractions of the i th species, X_i and Y_i , respectively, are given by

$$X_i = \frac{C_i}{\sum_{i=1}^{n_s} C_i}, \quad Y_i = \frac{\rho_i}{\rho} \quad (5)$$

The equation of state for the mixture is written as

$$P = R^0 T \sum_{i=1}^{n_s} C_i \quad (6)$$

where P is the pressure, T is the temperature, and R^0 is the universal gas constant. The specific total energy is the sum of the mixture-averaged specific internal energy, u , and the specific kinetic energy, written as

$$e_t = u + \frac{1}{2} \sum_{k=1}^d v_k v_k \quad (7)$$

where the former is the mass-weighted sum of the specific internal energies of each species, given by

$$u = \sum_{i=1}^{n_s} Y_i u_i \quad (8)$$

With the thermally perfect gas model, u_i is defined as

$$u_i = h_i - R_i T = h_{\text{ref},i} + \int_{T_{\text{ref}}}^T c_{p,i}(\tau) d\tau - R_i T \quad (9)$$

where h_i is the specific enthalpy of the i th species, $R_i = R^0/W_i$, T_{ref} is the reference temperature of 298.15 K, $h_{\text{ref},i}$ is the reference-state species formation enthalpy, and $c_{p,i}$ is the specific heat at constant pressure of the i th species, which is approximated with a polynomial as a function of temperature based on the NASA coefficients [30,31]:

$$c_{p,i} = \sum_{k=0}^{n_p} a_{ik} T^k \quad (10)$$

The flux can be expressed as the difference between the convective flux, \mathcal{F}^c , and the viscous flux, \mathcal{F}^v :

$$\mathcal{F}(y, \nabla y) = (\mathcal{F}^c(y) - \mathcal{F}^v(y, \nabla y)) \quad (11)$$

where the k th spatial components are defined as

$$\begin{aligned} \mathcal{F}_k^c(y) &= (\rho v_k v_1 + P \delta_{k1}, \dots, \rho v_k v_d + P \delta_{kd}, v_k (\rho e_t + P), \\ &\quad v_k C_1, \dots, v_k C_{n_s})^T \end{aligned} \quad (12)$$

$$\begin{aligned} \mathcal{F}_k^v(y, \nabla y) &= \left(\tau_{1k}, \dots, \tau_{dk}, \sum_{j=1}^d \tau_{kj} v_j + \sum_{i=1}^{n_s} W_i C_i h_i V_{ik} - q_k, \right. \\ &\quad \left. C_1 V_{1k}, \dots, C_{n_s} V_{n_s k} \right)^T \end{aligned} \quad (13)$$

τ is the viscous stress tensor, q is the heat flux, and V_{ik} is the k th spatial component of the diffusion velocity of the i th species, defined as

$$V_{ik} = \hat{V}_{ik} - \frac{\sum_{l=1}^{n_s} W_l C_l \hat{V}_{lk}}{\rho}, \quad \hat{V}_{ik} = \bar{D}_i \frac{\partial C_i}{\partial x_k} - \frac{\bar{D}_i}{\rho} \frac{\partial \rho}{\partial x_k} \quad (14)$$

which includes a standard correction to ensure mass conservation (i.e., $\sum_{i=1}^{n_s} W_i C_i V_{ik} = 0$) [32,33]. \bar{D}_i is the mixture-averaged diffusion coefficient of the i th species, obtained as [34]

$$\bar{D}_i = \frac{1}{\bar{W}} \frac{\sum_{j=1, j \neq i}^{n_s} X_j W_j}{\sum_{j=1, j \neq i}^{n_s} X_j / D_{ij}} \quad (15)$$

where $P_{\text{atm}} = 1 \text{ atm}$, $\bar{W} = \rho / \sum_i C_i$ is the mixture molecular weight, and D_{ij} is the binary diffusion coefficient between the i th and j th species, which is a positive function of temperature and pressure [35,36]. Note that \bar{D}_i can be nonzero for $C_i = 0$. The k th spatial components of the viscous stress tensor and the heat flux are written as

$$\begin{aligned} \tau_k(y, \nabla y) &= \mu \left(\frac{\partial v_1}{\partial x_k} + \frac{\partial v_k}{\partial x_1} - \delta_{k1} \frac{2}{3} \sum_{j=1}^d \frac{\partial v_j}{\partial x_j}, \dots, \frac{\partial v_d}{\partial x_k} + \frac{\partial v_k}{\partial x_d} \right. \\ &\quad \left. - \delta_{kd} \frac{2}{3} \sum_{j=1}^d \frac{\partial v_j}{\partial x_j} \right) \end{aligned} \quad (16)$$

where μ is the dynamic viscosity, calculated using the Wilke model [37], and

$$q_k(y, \nabla y) = -\lambda_T \frac{\partial T}{\partial x_k} \quad (17)$$

where λ_T is the thermal conductivity, computed with the Mathur model [38], respectively.

Equations (1–13) are solved using an extended version of the JENRE® Multiphysics Framework [39] that has been modified to include gas–solid coupling at the solid-fuel surface. The underlying flow solver chosen for this work utilizes a positivity-preserving and entropy-bounding nodal discontinuous Galerkin (DG) finite-element formulation [40], with two-dimensional axisymmetric DG discretization detailed in [39]. For these calculations, the HLLC approximate Riemann solver is used to compute the numerical flux across adjacent element faces, and the Bassi–Rebay (BR2) method [41] is used to discretize the viscous fluxes. Time integration was done explicitly using a 11-stage, 2nd-order strong stability-preserving Runge–Kutta method [42]. For the finite-rate kinetics simulations, reaction source terms are applied using a Strang-splitting approach, in which the system of stiff chemical reaction rate laws is integrated implicitly using the discrete Galerkin ordinary differential equation (DGODE) method as described by Johnson and Kercher [39].

An axisymmetric formulation of the DG discretization for multi-component, chemically reacting flows described by Johnson and Kercher [39] is used in this work to calculate the chemically reacting SFRJ flowfield. The spatial discretization error of the DG formulation has been verified to converge optimally with the expected rate of $(p+1)$ rate for multicomponent, chemically reacting flows [39]. It has been adapted for axisymmetric flows using the formulation given by Bassi et al. [43], demonstrating asymptotic convergence at the optimal rate. Final solutions in this work utilize DG $(p+1)$ elements, resulting in nominal second-order spatial and temporal accuracy.

B. Solid-Fuel Pyrolysis Model

For this work, we utilize a simplified model for the pyrolysis of the solid-fuel grain, as described in previous work [44], which assumes thermal equilibrium at the surface. This assumption eliminates the need to solve for the energy transport in the solid-fuel material, and the material interface condition reduces to a boundary condition for the gas-phase flow, which sets the temperature, density, and species mass fractions at the solid-fuel grain according to the following set of conservation equations:

$$\frac{\dot{m}_s}{W_{sg}} = C_{sg} u - \bar{D}_{sg} \left(\frac{\partial C_{sg}}{\partial n} - \frac{C_{sg}}{\rho} \frac{\partial \rho}{\partial n} \right) \quad (18)$$

$$0 = C_i u - \bar{D}_i \left(\frac{\partial C_i}{\partial n} - \frac{C_i}{\rho} \frac{\partial \rho}{\partial n} \right) \quad (19)$$

$$\dot{m}_s L = -k_f \left(\frac{\partial T}{\partial n} \right)_f \quad (20)$$

Table 1 HTPB pyrolysis parameters [13,45]

Parameter	Value
A_p	$5.65 \times 10^7 \text{ J/(k} \cdot \text{mol)}$
E_p	$4.0889 \times 10^4 \text{ s}^{-1}$
l_r	$6 \times 10^5 \text{ m}$

Table 2 Thermophysical properties of model HTPB [13,45]

Density	Specific heat	Thermal conductivity	Heat of formation
900 kg/m ³	1100 J/(kg · K)	0.235 W/m K	54.4 kJ/kg

where the subscripts s , sg , and f refer to the solid phase, gas-phase pyrolysis product species, and the fluid region, respectively. The equations enforce the conservation of mass, species, and energy across the interface, with the left- and right-hand sides representing the solid phase and gas phase, respectively. The temperature-dependent latent heat of vaporization is then defined as the difference between the solid-phase and gas-phase enthalpies, $L = h_s - h_{sg}$. The enthalpy of the solid-fuel material is related to temperature via an equation of state, $h_s = C_p T_I + e_0$, where C_p is the specific heat of the material, T_I is the temperature at the fluid–solid interface, and e_0 is a reference energy that enforces consistency with the gas-phase equation of state for the corresponding vapor species. The surface blowing velocity is $u = \dot{m}_s/\rho$, where ρ is the density of the gas in the pyrolysis zone. The regression rate \dot{r} is modeled based on an Arrhenius rate form:

$$\dot{m}_s = \rho_s l_r A_p e^{-E_p/R^0 T_I} \quad (21)$$

where \dot{m}_s is the mass flux of fuel into the fluid region and l_r is the thickness of the pyrolysis zone. A_p and E_p are empirical fits for the pre-exponential factor and activation energy, respectively, given in Table 1. By assuming thermal equilibrium with the fuel surface, the interface temperature can instantaneously adjust to the imposed thermal gradient at the boundary. In reality the interface has some thermal mass, resulting in a phase delay between the imposed gradient and resulting interface temperature. Using this model, the variance of the local regression rate will increase, but the average regression rate will be consistent.

We consider a solid fuel composed entirely of a hypothetical polymer with properties similar to HTPB that is converted to the gaseous hydrocarbon 1,3-butadiene (C_4H_6). Table 2 gives the thermophysical properties used to model the HTPB solid fuel from Arisawa and Brill [13,45]. Equations (18–21) then define a set of $n_s + 1$ nonlinear equations for the concentrations of the n_s gas-phase species in the model and the interface temperature, which are solved using an iterative Gauss–Newton method.

C. Chemical Kinetics Models

Combustion is modeled using finite-rate chemical kinetics, where the net production of each species i , ω_i , is calculated by

$$\omega_i = \sum_{j=1}^{n_r} \nu_{ij} \Omega_j \prod_{k=1}^{n_s} C_k^{b_{k,j}} \quad (22)$$

for a system of n_r chemical reactions with stoichiometric coefficients ν_{ij} and reaction order coefficients $b_{k,j}$ associated with the j th reaction. C_k is the concentration of the k th species. The rate of progress for reaction j , Ω_j , takes an Arrhenius form:

$$\Omega_j = A_j T^{\beta_j} \exp(-E_{a,j}/R^0 T) \quad (23)$$

where A_j , β_j , and $E_{a,j}$ are associated model coefficients corresponding to the pre-exponential factor, temperature exponent, and activation energy for reaction j , respectively. For ease of describing and analyzing the chemical kinetics, the forward reaction rate for the j th reaction, r_{fj} , is defined as

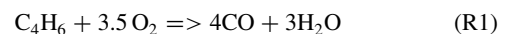
$$r_{fj} = A_j T^{\beta_j} \exp(-E_{a,j}/RT) \prod_{k=1}^{n_s} C_k^{b_{k,j}} \quad (24)$$

where $\omega_i = \sum_{j=1}^{n_r} \nu_{ij} (r_{fj} - r_{bj})$, and r_{bj} is the backward reaction rate for reversible reactions, computed using an equilibrium constant approach [46]. Casting in the form of Eq. (24) demonstrates that calibration of the finite-rate chemistry can be achieved through modification of A_j , β_j , $E_{a,j}$, and $b_{k,j}$. For nonelementary reactions, the reaction orders of each species, $b_{k,j}$, is not necessarily equivalent to the stoichiometric coefficient but instead can take on an arbitrary value necessary to reproduce empirical flame trends. The selection of each model parameter has an important consequence on the overall performance and stability of a given reaction mechanism.

A two-step global combustion mechanism and a six-step global combustion mechanism are introduced, and starting reaction rates are taken from the existing literature, mainly for 1,3-butadiene oxidation with pure O₂ in HRE applications. To serve as a baseline for all 1D and 2D calculations, a modified 109-step/20-species pressure comprehensive skeletal mechanism, developed by Ciottoli et al. [47], is used to evaluate the global 1,3-butadiene chemistry models. Validation of the skeletal mechanism in the original works is performed for a series of 1,3-butadiene laminar flames against a detailed 2583-step/561-species mechanism developed by Curran et al. for *n*-heptane combustion [48].

1. Two-Step Reaction Mechanism

The global two-step/six-species reaction mechanism is presented for 1,3-butadiene [28]. The two-step global reaction mechanism consists of six species: C₄H₆, H₂O, CO₂, CO, O₂, and inert N₂. The mechanism consists of one reaction for the oxidation of C₄H₆ and one reversible reaction for the oxidation of CO to CO₂:



The reaction rates for the two-step reaction mechanism are shown in Table 3. The reversible reaction rate for the CO oxidation is calculated explicitly due to the specified nonreactant reaction orders. The rate parameters for the reverse reaction were calculated using a standard thermochemical-equilibrium approach.

The reaction orders for the C₄H₆ oxidation ($b_{1,1} = 0.25$, $b_{2,1} = 1.5$) are from the original Westbrook and Dryer formulation despite the numerical instabilities caused by reaction orders lower than one. Reaction orders below one on the fuel are necessary to obtain the correct flame trends in the fuel-rich region [49]. The sum of reaction orders for the C₄H₆ oxidation $b_{1,1} + b_{2,1} = 1.75$ is necessary for

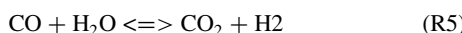
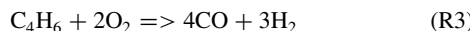
Table 3 Starting reaction rates for two-step global mechanism

Reaction	Forward reaction rate	Source
(R1)	$r_{f1} = 1.35 \cdot 10^{10} \exp(-30000/R, T)[\text{C}_4\text{H}_6]^{25}[\text{O}_2]^{1.5}$	Morinigo et al. [25]
(R2)	$r_{f2} = 2.24 \cdot 10^{12} \exp(-12000/R, T)[\text{CO}]^{1.0}[\text{H}_2\text{O}]^{0.5}[\text{O}_2]^{0.25}$	Andersen et al. [50]
(R2r)	$r_{b2} = 5.0 \cdot 10^8 \exp(-77200/R, T)[\text{CO}_2]$	Calculated

enforcing pressure dependence through the equilibrium partial pressures. Increased numerical stiffness arises from the use of non-integer reaction orders, particularly for reaction orders below unity.

2. Six-Step Reaction Mechanism

The global 6-step/10-species reaction mechanism is presented for 1,3-butadiene [29]. The reaction mechanism consists of 10 species: C₄H₆, H₂O, CO₂, CO, O₂, OH, O, H, H₂, and inert N₂. Reactions (R3) and (R4) consist of two breakdown pathways of 1,3-butadiene into intermediates CO and H₂. Reaction (R5) is the well-studied water-phase shift reaction that serves as the only pathway for the complete oxidation of CO to CO₂. Reaction (R6) controls the rate of oxidation of H₂ into H₂O. Reactions (R7) and (R8) are recombination reactions that introduce radicals O, H and OH to mitigate temperature rise:



The reaction rates for the six-step reaction mechanism are shown in Table 4. Similar to the two-step reaction mechanism, the reaction orders for (R3) ($b_{1,3} = 0.5$, $b_{2,3} = 1.25$) remain faithful to the original Jones and Lindstedt formulation to maintain both physically realistic pressure dependency and correct fuel-rich dependency. The reaction orders for (R6) ($b_{1,6} = 0.25$, $b_{2,6} = 1.5$), from Andersen et al. [50], introduce additional numerical stiffness that manifests itself in stability issues in the solution of steady-state flames through Newton's and other iterative method approaches. The radical recombination reactions (R7) and (R8) are pertinent to accurate prediction of temperature by modulating high-temperature specific heats. The added complexity of the six-step mechanism is justified to compute additional important flame intermediates and accurately predict a high-temperature combustion phenomenon.

3. Equilibrium Calculations

Equilibrium composition calculations of 1,3-butadiene and air are performed using an adiabatic Gibbs solver in CANTERA [36]. The calculations hold irrespective of updated pre-exponential Arrhenius factors, as the equilibrium composition is calculated based on the thermodynamic properties of the mixture alone. Figure 1 shows the equilibrium temperature and composition for an unburnt mixture of fuel and air at pressures of 1 and 10 atm and temperatures of 300 and 600 K. There is a negligible difference in the prediction of major species and adiabatic flame temperature between the 6-step mechanism and the 20-species skeletal mechanism. This can be attributed to the inclusion of intermediate species OH, O, H₂, and H in the six-step mechanism, providing a means for mitigating the adiabatic

flame temperature through dissociation. There is a clear discrepancy in the prediction of adiabatic flame temperature and major species by the two-step reaction mechanism. The two-step mechanism does not include any intermediate species for the dissociation of H₂O, leading to the overprediction of H₂O mole fraction and overall combustion progress. The problem is aggravated in the fuel-rich regions, in which the overprediction of H₂O is largest, consequently leading to inadequate prediction of CO and CO₂ mole fraction. The two-step mechanism predicts the equilibrium major species and adiabatic flame temperature in the fuel-lean branch reasonably well and approaches the true adiabatic flame temperature in the higher-pressure cases. This leads to some favorable utility in the prediction of high-pressure combustion in SFRJs. However, the above-mentioned inherent limitations must be taken into account when choosing to use the heavily simplified two-step mechanism. Overprediction of thermal efficiency and combustion performance is expected as a result of omitting the inclusion of several key species and reaction pathways. Further, accurate prediction of equilibrium composition and temperature are necessary prerequisites for the accurate calculation of flame speeds, extinction limits, and combustion dynamics.

III. Model Calibration

For HTPB/air combustion in SFRJ applications, the reduced-order models need to be accurate across a variety of operating altitudes and Mach numbers, be proficient in modeling the partially premixed gas-phase combustion regime, and provide robust and accurate performance when coupled with solid-fuel pyrolysis models. In order to capture these features, model calibration based on laminar flame speed, ignition delay, and extinction strain rate is considered.

Laminar flame speed s_L and ignition delay τ are extensively studied for partially premixed combustion systems. Previous work [44] has shown that global mechanisms for 1,3-butadiene combustion fit for laminar flame speed perform inadequately at mitigating the peak flame temperatures and predicting the major flame-marking species in solid-fuel counterflow flames. As a result, the coupling of the global reaction mechanisms and pyrolysis boundary conditions leads to inadequate predictions of the fuel regression rate. Sensitivity coefficients based on laminar flame speed, $S_{s_L} = \ln(s_L^+ / s_L^-) / \ln(2.0 / 0.5)$, are presented in the Appendix for reference in future calibrations. Figure 2 shows the failure of the global mechanisms to capture ignition delay times or trends as compared to the skeletal mechanism. The absence of any chain-branching reactions lead the global mechanisms to be ill-suited at predicting ignition delays, with insensitivity to changes in Arrhenius rate parameters. Changing the pre-exponential parameter rates does induce a shift in the ignition delay time but is still unable to capture the ignition delay trend with increasing temperature.

Given these limitations, this study utilizes the extinction strain rate in strained counterflow diffusion flames as the main target for calibration of the global reaction mechanisms. Extinction strain rate is found to be a suitable metric to calibrate reduced-order mechanisms, evidenced by the reproduction of flame dynamics in both the SFRJ recirculation zone and downstream diffusion regions. Final model calibration is performed iteratively, with the extinction strain rate used to calibrate the highly sensitive reactions in each mechanism. Next, the nonsensitive reactions are calibrated to best match the maximum temperature and flame structure in the strained

Table 4 Starting reaction rates for six-step global mechanism

Reaction	Forward reaction rate	Source
(R3)	$r_{R3} = 4.2 \cdot 10^{11} \exp(-30000/R, T)[\text{C}_4\text{H}_6]^5[\text{O}_2]^{1.25}$	Morinigo et al. [25]
(R4)	$r_{R4} = 3.0 \cdot 10^8 \exp(-30000/R, T)[\text{C}_4\text{H}_6][\text{H}_2\text{O}]$	Morinigo et al. [25]
(R5)	$r_{R5} = 2.75 \cdot 10^9 \exp(-20000/R, T)[\text{CO}][\text{H}_2\text{O}]$	Morinigo et al. [25]
(R6)	$r_{R6} = 6.8 \cdot 10^{15} \cdot T^{-1} \exp(-40000/R, T)[\text{H}_2]^{0.25}[\text{O}_2]^{1.5}$	Andersen et al. [50]
(R6r)	$r_{R6r} = 1.255 \cdot 10^{17} \cdot T^{-0.877} \exp(-97900/R, T)[\text{H}_2]^{-0.75}[\text{O}_2][\text{H}_2\text{O}]$	Andersen et al. [50]
(R7)	$r_{R7} = 1.5 \cdot 10^9 \exp(-113000/R, T)[\text{O}_2]$	Morinigo et al. [25]
(R8)	$r_{R8} = 2.3 \cdot 10^{22} \cdot T^{-3} \exp(-120000/R, T)[\text{H}_2\text{O}]$	Morinigo et al. [25]

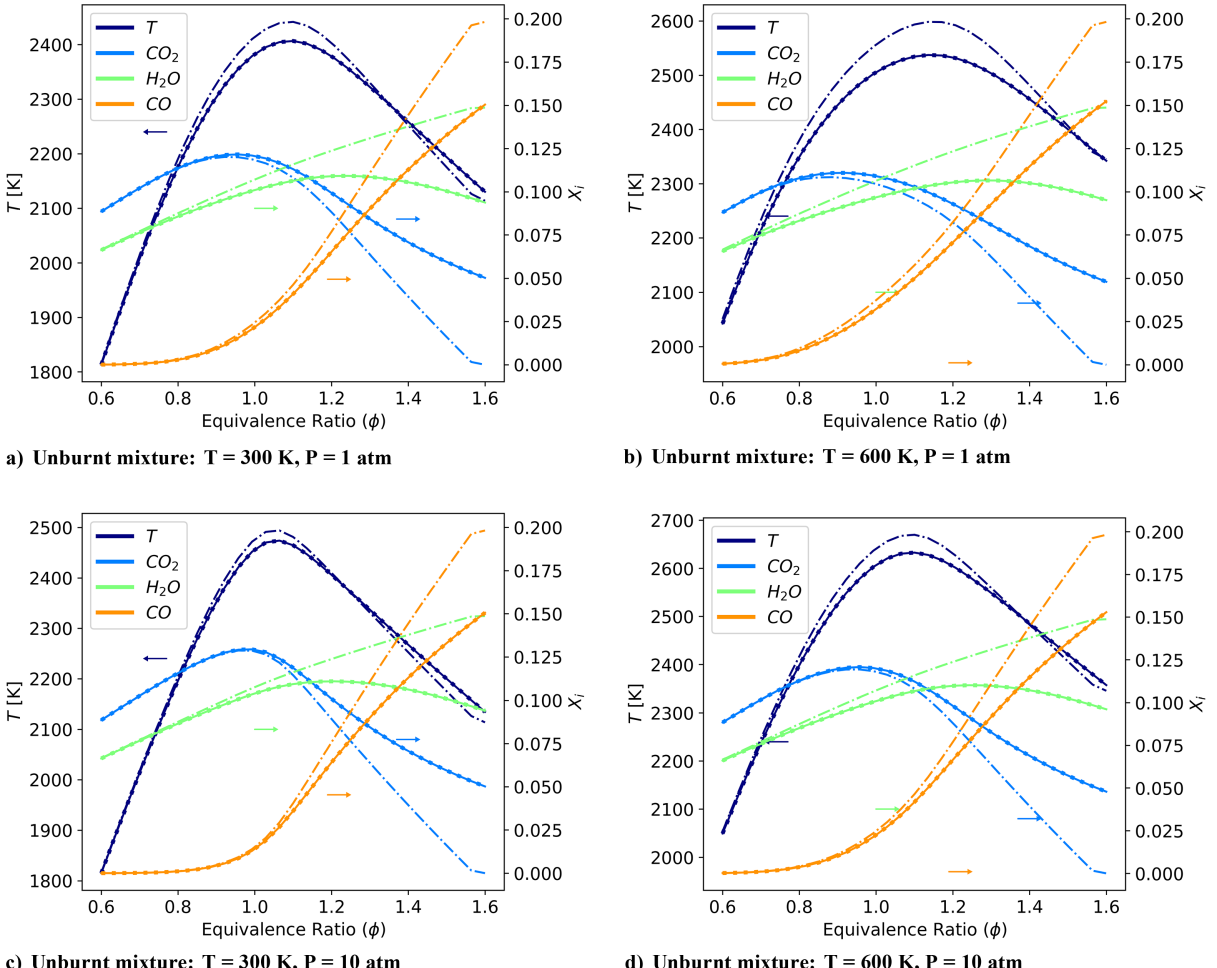


Fig. 1 Equilibrium temperature and composition comparison for 2-step mechanism (dashed-dotted), 6-step mechanism (dotted), and 20-species skeletal mechanism [47] (solid).

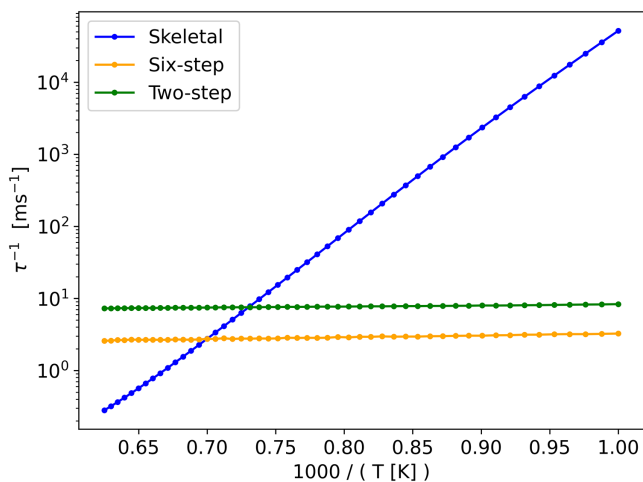


Fig. 2 Comparison of ignition delay time prediction with reduced mechanisms.

flame cases. The high pressure, $p = 5$ and 10 atm, cases are weighted higher than the atmospheric pressure case to ensure the reduced mechanisms are better calibrated for the conditions found in practical SFRJ engines.

1. Sensitivity Analysis

Before model calibration, sensitivity analyses [51] were carried out for the two-step and six-step global reaction mechanisms to

identify the key reactions affecting the mean extinction strain rate, a_e , where $a = (u_f + u_o)/L$. One-dimensional flames are simulated in CANTERA using the Counterflow Diffusion Flame (CDF) solver [36]. The fuel inlet contains pure C_4H_6 at an elevated temperature of 650 K, a typical surface temperature for solid-fuel pyrolysis. The oxidizer inlet contains air also at 650 K, separated from the fuel inlet by 10 mm. The pre-exponential factor A_j in the Arrhenius rate expressions was increased and decreased by a factor of two, and the new laminar flame speed was recorded. The sensitivity coefficient for a given reaction step, S [19], is defined as

$$S = \frac{\ln(a_e^+ / a_e^-)}{\ln(2.0 / 0.5)} \quad (25)$$

where a_e^+ is the extinction strain rate calculated with the increased pre-exponential factor and a_e^- is the extinction strain rate calculated with the decreased pre-exponential factor. Each pre-exponential factor is modified individually, and a sensitivity coefficient is calculated for each reaction to determine the relative sensitivity. A positive sensitivity coefficient indicates that an increase in the pre-exponential factor increases the extinction strain rate, while a negative sensitivity coefficient shows an increase in the pre-exponential factor decreases the extinction strain rate. Sensitivity coefficients for the two-step and six-step mechanisms are normalized independently.

Figure 3 shows the results of the sensitivity analysis for extinction strain rate at varying surrounding pressures of 1, 5, and 10 atm. For the two-step global reaction mechanism and for all pressures, reaction (R1) shows the greatest sensitivity, which is a consequence of this reaction containing the majority of heat release. Reaction (R2)

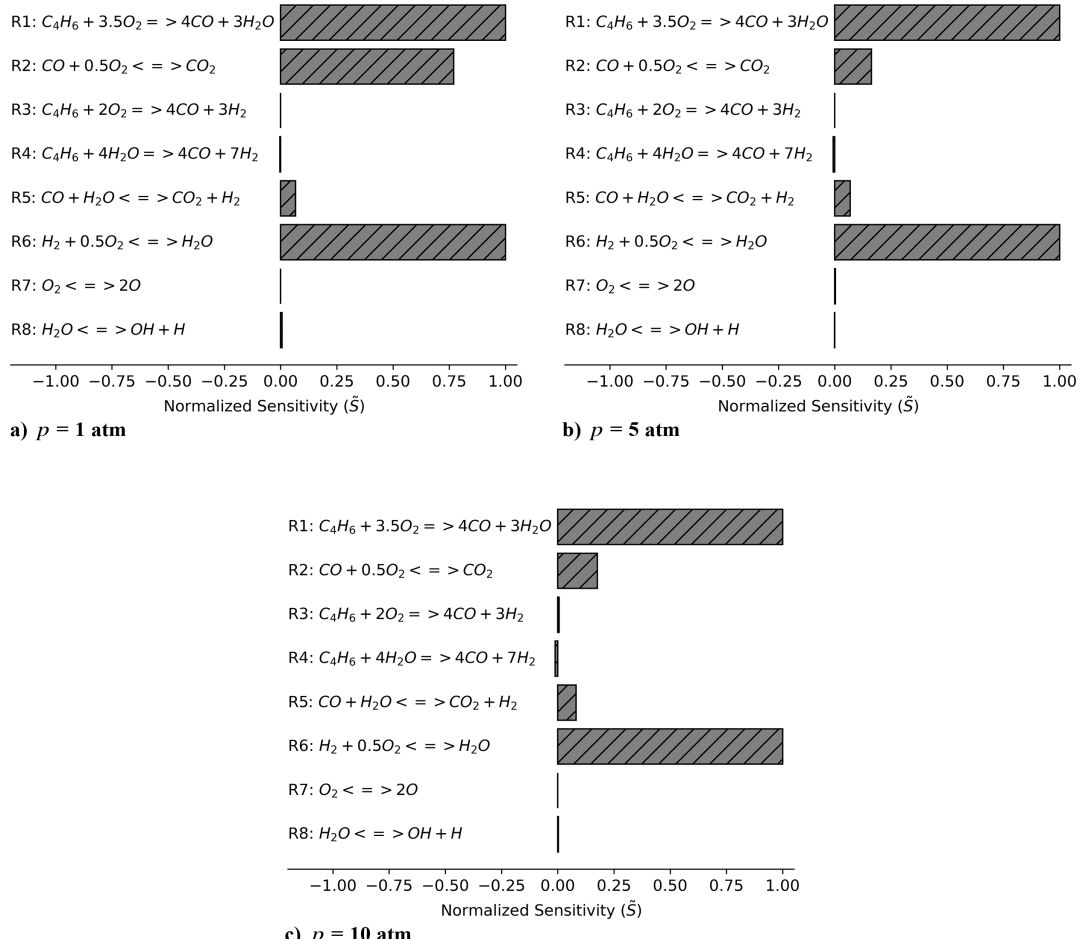


Fig. 3 Brute-force sensitivity analysis of two-step and six-step reaction mechanisms based on extinction strain rate.

shows higher sensitivity at low pressure and lower sensitivity at higher pressure, which allows a precise tuning of extinction strain rates across pressure. For the six-step global reaction mechanism, the sensitivity coefficients are relatively insensitive across ambient pressure conditions. The extinction strain rate is dominated by reaction R6, which controls the rate of H₂ oxidation to H₂O that carries a large fraction of the total heat release. Reaction (R5), the water-gas shift reaction, has the next largest sensitivity coefficient as it controls the oxidation of CO to CO₂ and couples with reaction (R6). As expected, the recombination reactions have near-zero sensitivity. Interestingly, the fuel decomposition reactions (R3) and (R4) have near-zero sensitivity as a result of the bulk heat release resulting from reactions (R5) and (R6). By determining reactions sensitive to the target metric, nonsensitive reactions can be tuned to secondary metrics of interest. Reaction rates for the calibrated two- and six-step mechanisms are shown in Tables 5 and 6, respectively.

Figure 4 shows the maximum temperature as a function of the mean strain rate at varying ambient pressures of 1, 5, and 10 atm for the calibrated combustion models. The calibrated models demonstrate noteworthy pressure dependence and agreeable temperature prediction with respect to the skeletal model. The models demonstrate better prediction at higher pressures that are typical of standard SFRJ operation. For the two-step mechanism, the change in

Table 5 Fit reaction rates for two-step global mechanism

Reaction	Forward reaction rate
(R1m)	$r_{f1m} = 2.7093 \cdot 10^{10} \exp(-30000/R, T)[C_4H_6]^{2.25}[O_2]^{1.5}$
(R2)	$r_{f2} = 1.12 \cdot 10^7 \exp(-12000/R, T)[CO]^{1.0}[H_2O]^{0.5}[O_2]^{0.25}$
(R2r)	$r_{b2} = 2.5 \cdot 10^3 \exp(-77200/R, T)[CO_2]$

Table 6 Fit reaction rates for six-step global mechanism

Reaction	Forward reaction rate
(R3)	$r_{R3} = 1.32 \cdot 10^{12} \exp(-30000/R, T)[C_4H_6]^5[O_2]^{1.25}$
(R4)	$r_{R4} = 8.0 \cdot 10^8 \exp(-30000/R, T)[C_4H_6][H_2O]$
(R5m)	$r_{R5m} = 1.5 \cdot 10^{10} \exp(-20000/R, T)[CO][H_2O]$
(R6m)	$r_{R6m} = 2.64 \cdot 10^{15} \cdot T^{-1} \exp(-40000/R, T)[H_2]^{0.25}[O_2]^{1.5}$
(R6rm)	$r_{R6rm} = 4.84 \cdot 10^{16} \cdot T^{-0.877} \exp(-97900/R, T)[H_2]^{-0.75}[O_2][H_2O]$
(R7)	$r_{R7} = 1.5 \cdot 10^{10} \exp(-113000/R, T)[O_2]$
(R8)	$r_{R8} = 2.3 \cdot 10^{23} \cdot T^{-3} \exp(-120000/R, T)[H_2O]$

sensitivity across pressure allows for excellent tuning to the extinction strain rate of the skeletal mechanism. The two-step mechanism over-predicts the maximum flame temperature in the low-strain cases and under-predicts the temperature for the high-strain cases. The two-step mechanism is not able to capture the same trend in maximum flame temperature, having much larger gradients in temperature compared to the skeletal mechanism. The six-step mechanism, on the other hand, shows improved agreement with the skeletal mechanism extinction strain rate across all pressures, with excellent agreement at 5 and 10 atm. The six-step mechanism is able to capture the maximum flame temperature trend with increasing strain rate, with the best agreement at 10 atm. Both mechanisms consistently over-predict temperature at low strain rates, particularly at low pressure.

IV. Results and Discussion

A. One-Dimensional Solid-Fuel Counterflow Formulation

A series of 1D solid-fuel counterflow flames are simulated in CANTERA using the Counterflow Diffusion Flame (CDF)

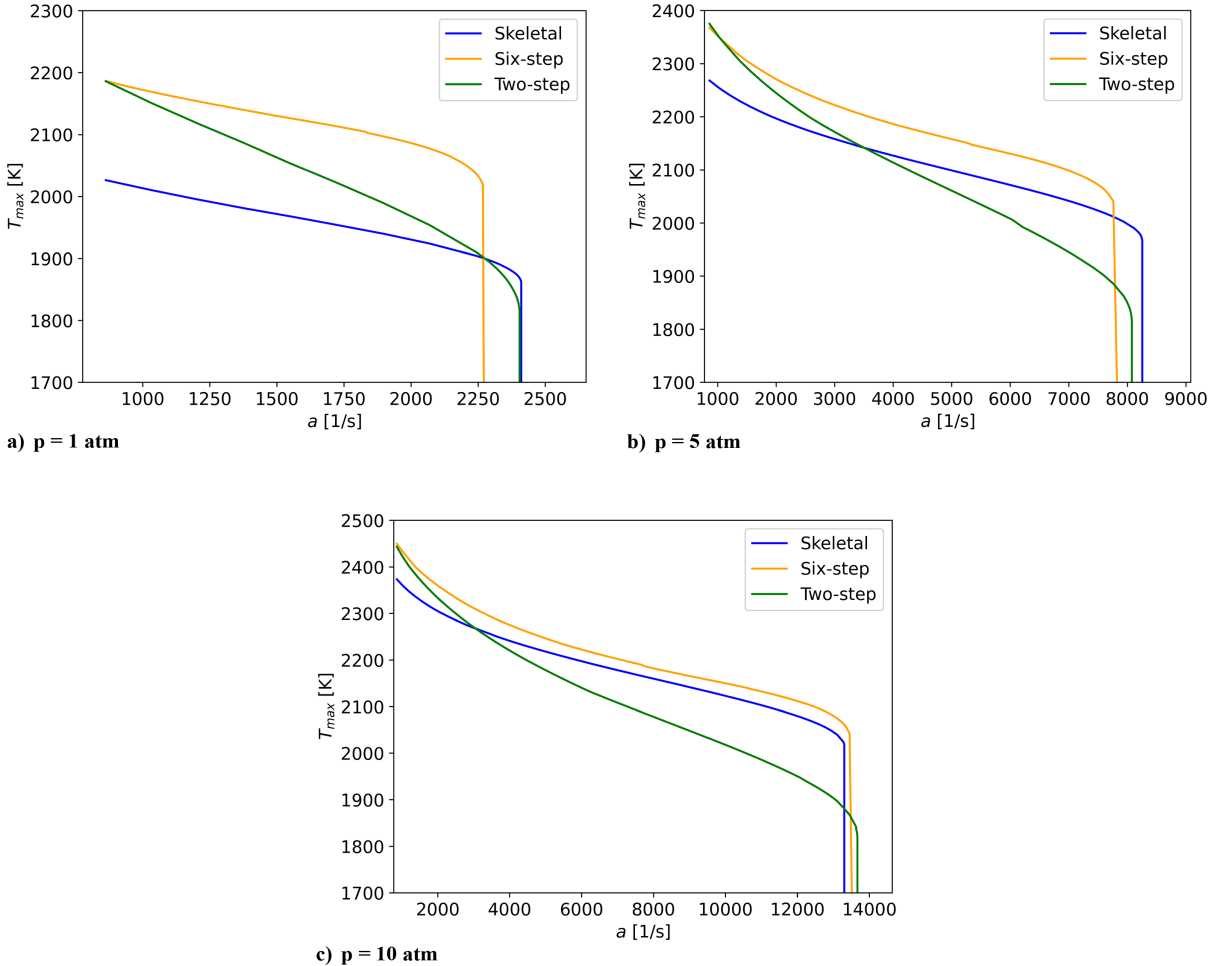


Fig. 4 Final calibrated model extinction strain rate curves.

solver [36] to evaluate the calibrated model prediction on flame structure and its coupling with HTPB pyrolysis. One-dimensional solid-fuel counterflow simulations represent the limiting case for SFRJ combustion. A fully coupled solid-fuel boundary condition is used to define the fuel mass flux, pyrolysis gases, and surface temperature of the HTPB fuel grain [52]. The conservation of mass, species, and energy at the boundary are defined as

$$\dot{m}_s = \rho u = \rho_s \dot{r} \quad (26)$$

$$\dot{m}_s = \rho u Y_{sg} - \rho_s D_F \left(\frac{\partial Y_{sg}}{\partial z} \right)_f \quad (27)$$

$$0 = \rho u Y_i - \rho D_i \left(\frac{\partial Y_i}{\partial z} \right)_f \quad (28)$$

$$\dot{m}_s L_v = -k_f \left(\frac{\partial T}{\partial z} \right)_f \quad (29)$$

where the equations follow the same form as Eqs. (18–21) but are expressed in terms of species mass fraction. The regression rate \dot{r} is modeled based on an Arrhenius rate form:

$$\dot{r} = A e^{-\frac{E_a}{RT_s}} \quad (30)$$

where A and E_a are empirical fits for the pre-exponential factor and activation energy, respectively, given in previous work [52]. We again consider a solid fuel composed entirely of a hypothetical polymer with properties similar to HTPB that is converted to the gaseous hydrocarbon 1,3-butadiene (C_4H_6). Equations (26–30) are

solved using an iterative Gauss–Newton method outside of the CDF solver, and the fuel boundary condition is updated to reflect conservation. The gas-phase solution is subsequently recalculated until convergence is met.

Table 7 summarizes the test case conditions used to evaluate the reduced-chemical kinetics models. The oxidizer inlet has a separation distance D of 10 mm from the solid-fuel boundary. For all simulations, air at 650 K at a velocity of 20 m/s is incident on the solid-fuel surface, representing a typical SFRJ inflow temperature under moderate strain. Pressure is increased from 1 to 10 atm to assess the performance of the reduced chemical kinetics models. This results in having the same mean strain rate $a_s = u_o/L = 2000 \text{ s}^{-1}$ across all pressure conditions, but with increasing mass flux of air due to increasing density with pressure. Flame thickness ℓ is measured as the distance between the fuel grain surface and a temperature threshold, selected to match closely with experimental shadowgraph results found in previous work [52]. Numerical simulations using a detailed 613-step/92-species high-temperature kinetics mechanism for 1,3-butadiene combustion, developed by Laskin, Wang, and Law [18], are also performed to serve as a baseline for evaluating the coupling between the gas-phase kinetics and solid-fuel pyrolysis boundary condition.

Table 7 One-dimensional solid-fuel counterflow conditions

Parameter	Value
D , mm	10
Oxidizer composition, X	$O_2: 0.23, N_2: 0.76$
Oxidizer temperature, K	650
Pressure, atm	1–10

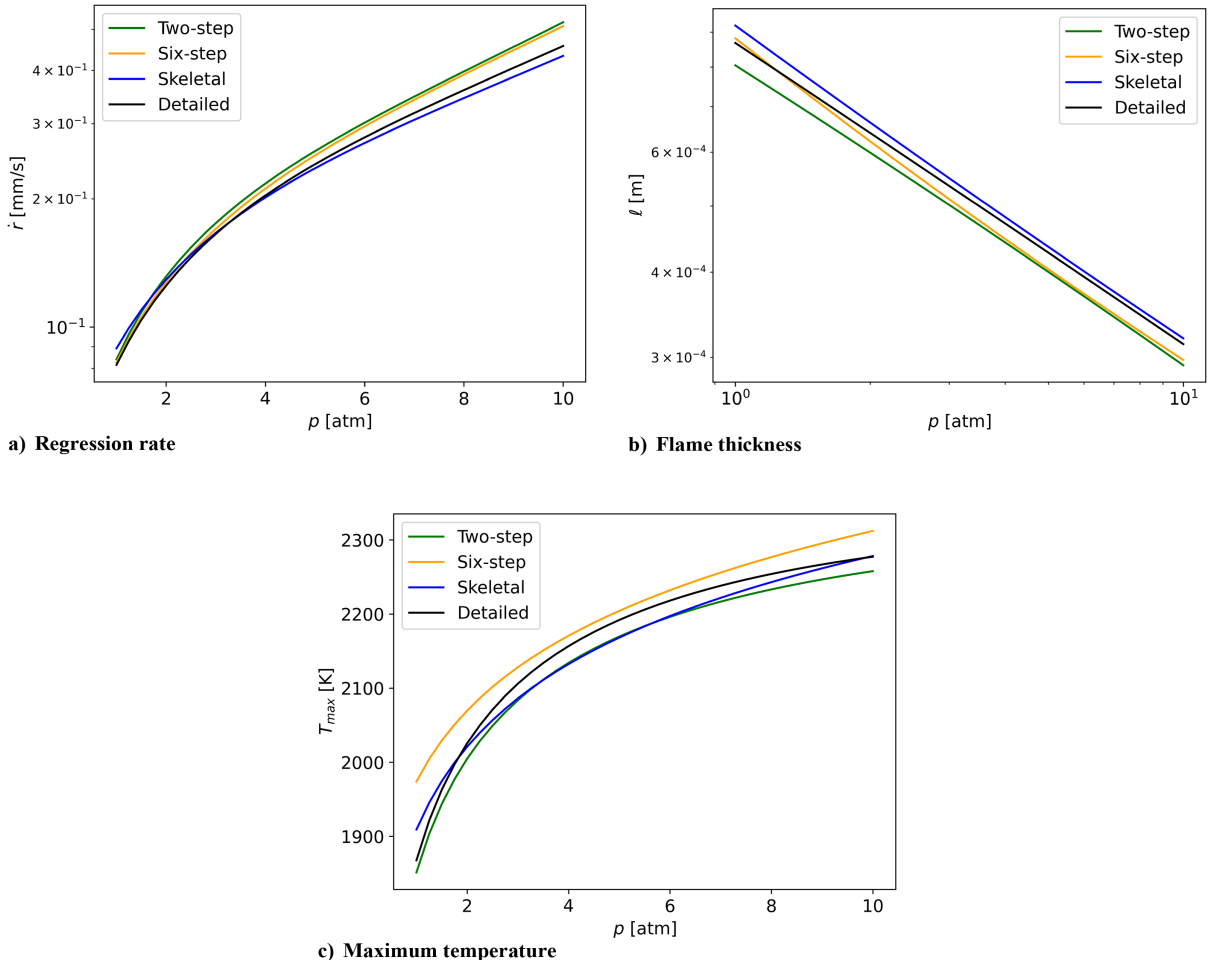


Fig. 5 Prediction of flame trends with increasing pressure in 1D solid-fuel counterflow flame.

Figure 5 shows the predicted regression rates, flame thicknesses, and maximum flame temperatures of the reduced global mechanisms with the skeletal mechanism. To give context to the observed trends and provide valuable major species information, the flame structure at a representative pressure of 10 atm is shown in Fig. 6. Excellent agreement with the detailed mechanism validates the

skeletal mechanism as a suitable baseline for evaluating the prediction of flames with interfacial HTPB pyrolysis coupling.

Both two-step and six-step mechanisms are able to accurately reproduce the regression rate of HTPB and show good agreement with the skeletal mechanism. The six-step mechanism shows improved agreement with the skeletal mechanism over the two-step

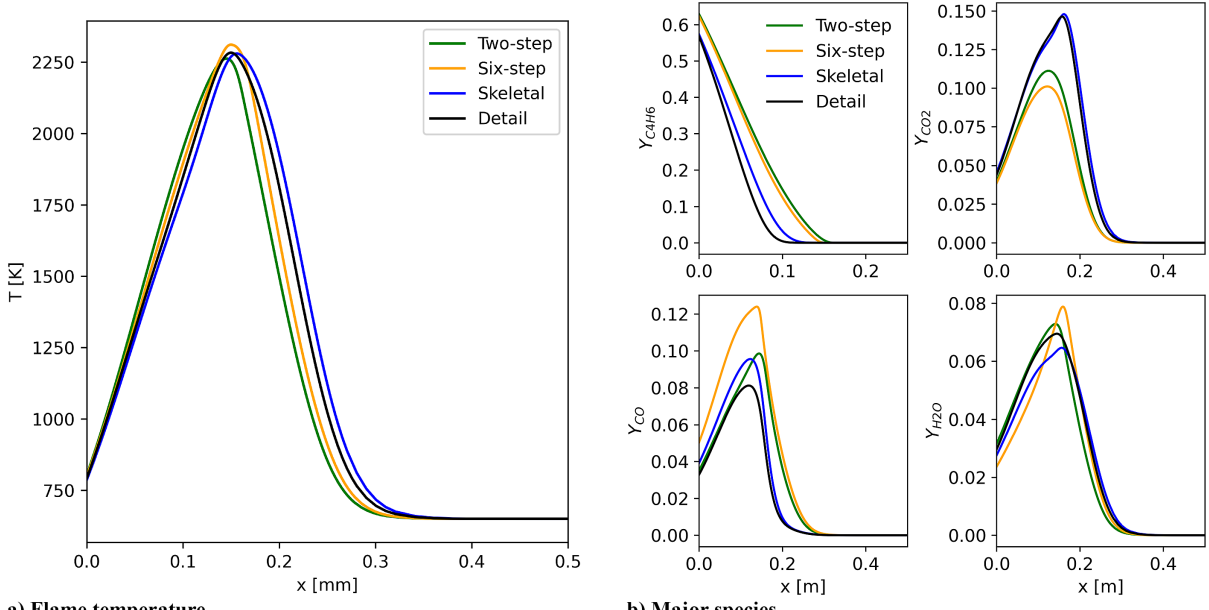


Fig. 6 Prediction of flame structure in 1D solid-fuel counterflow by reaction mechanism, $p = 10$ atm.

mechanism. The local temperature gradient at the wall is larger for the two-step mechanism, resulting in slight overprediction of regression and fuel surface temperature. This is understood as the two-step mechanism having a faster consumption of C_4H_6 and production of CO_2 and H_2O as compared to the six-step mechanism, resulting in higher heat release and a larger temperature gradient on the fuel-rich side. The inclusion of a secondary endothermic fuel breakdown reaction (R4) in the six-step mechanism seems to minimize the temperature gradient, even with slightly higher maximum flame temperature prediction. A large portion of the heat release for the six-step mechanism is found to occur due to the oxidation of H_2 to H_2O in (R6), which occurs within a thinner region closer to the max flame temperature.

The reduced global mechanisms show excellent agreement in flame thickness with the skeletal mechanism. Flame thickness is an important property for accurately reproducing the flame structure in highly turbulent configurations, as found in SFRJ combustors. Thicker flames have been shown to be less sensitive to small eddies, thereby decreasing the level of turbulence-induced flame wrinkling [53]. The maximum temperature shows good agreement with the skeletal mechanism for both reduced mechanisms. The two-step mechanism actually has slightly better maximum temperature prediction for this moderately strained case as compared to the six-step mechanism. Even with accurate flame thickness prediction and temperature prediction, the two-step mechanism still slightly overpredicts regression rates due to the heavily reduced chemical kinetics. The inclusion of additional fuel oxidation pathways and fuel breakdown reactions results in an increase in the heat release zone width, which benefits the prediction of physically accurate temperature gradients [44].

The two-step and six-step reaction mechanisms are able to accurately reproduce the C_4H_6 mass fraction at the solid–gas interface. Due to the lack of endothermic fuel breakdown reactions, higher levels of C_4H_6 mass fraction are observed through the flame. The two-step mechanism does an excellent job predicting the major species, particularly the CO mass fraction. The six-step mechanism performs well in capturing the oxidation of H_2O , but is less accurate in capturing the CO to CO_2 oxidation. Both mechanisms reproduce the interface composition predicted by the skeletal mechanism with an impressive agreement.

B. Two-Dimensional Axisymmetric SFRJ Simulations

Evaluation of the calibrated reduced-order kinetics models is performed by assessing LES simulations of a model SFRJ engine against the skeletal mechanism. Figure 7 shows the axisymmetric SFRJ geometry, based on the experimental work of Veraar et al. [54], with boundary conditions colored. Heated vitiated air is introduced to the inflow of the domain, where it is accelerated through the converging inlet section. Combustion is sustained through a sudden expansion between the port and inlet areas (A_p/A_{in}). The fuel grain has a length $L = 30$ cm, followed by an aft-mixing section to enhance combustion stability. The flow accelerates through the nozzle down to the choked exhaust, with the computational domain terminating at the nozzle throat. Inlet and nozzle walls are modeled as no-slip isothermal walls at 650 and 1000 K, respectively. The fuel grain surface is modeled via Eqs. (18–20), and a supersonic outflow condition is specified at the exhaust. Details of the experimental inlet conditions and geometry of the model solid-fuel ramjet are given in Table 8. The computational geometry matches the experimental geometry, but with an assumption that

Table 8 Experimental conditions and geometry of model SFRJ [54]

Parameter	Value
T_{in} , K	614
\dot{m}_{air} , g/s	906
P_{comb} , bar	6.4
L , cm	30
A_p/A_{in}	4.35
A_p/A_t	1.93
d_p , mm	62.6
c^* , m/s	1050

the fuel grain surface is static during the numerical simulation sampling time. The geometry, elevated operating pressure, high-velocity air, and pyrolysis boundary condition result in an extremely challenging and relevant environment to test the reduced chemistry models. The throat area A_t is larger than the inlet area A_{in} , requiring the engine to choke due to the combined effect of increased mass flux of fuel from the pyrolyzing surface and heat addition from gas-phase combustion. Back pressure is imposed during the initial startup and transient phases and subsequently reduced until the flow is choked and a supersonic outflow condition is maintained. A high-viscosity sponge layer is utilized just upstream of the nozzle throat to help condition the flow before the exhaust.

Reactions are initiated by introducing a high-temperature ignition kernel in the region just behind the step. Two flow-through times are allowed before quasi-steady-state combustion and pyrolysis are established and sampling of the solution for further analysis. Numerical simulations are sampled for a total of 3 ms at 166.67 kHz, using a time step $\Delta t = 15$ ns. This corresponds to a CFL number of approximately 1.5 and a total sample duration of 3 flow-through times, defined as the total length of the combustor divided by the inlet velocity. This duration is insufficient to provide accurate converged average quantities, which require a sampling time considerably longer than what is represented in this work due to the long residence time in the recirculation zones. However, selected average quantities are shown to sufficiently illustrate trends and provide bounding intervals.

The experimental system of Veraar et al. made use of a medium-temperature vitiator (MTV) [54], which uses a hydrogen flame to increase the temperature of the inlet air stream. The necessary mass fraction of oxygen was replaced to maintain an equivalent mass fraction of oxygen with air at $Y = 0.232$. To determine the inflow composition, an adiabatic Gibbs solver in CANTERA [36] is used to iteratively calculate the temperature and corresponding composition. Assuming no heat losses through the MTV and considering only major species, the inflow species composition from the MTV is

Table 9 Inflow species composition from MTV

Species	Mass fraction
O_2	0.232
N_2	0.742
H_2O	0.026

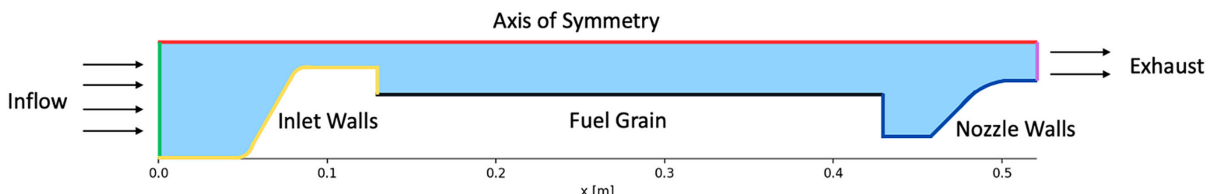


Fig. 7 Axisymmetric model solid-fuel ramjet. Experimental data is used to specify the stagnation properties, $T_t = 673.1$ K and $P_t = 8.975$ MPa, which define the inlet conditions [54].

given by Table 9. Although the mass fraction of water is small, $Y = 0.026$, the inclusion of even small amounts of water in high-pressure combustion has been shown to significantly lower activation energy through enhanced chemical kinetics pathways [55].

C. Model Verification Studies

1. The $h-p$ Refinement Study

An $h-p$ refinement study is performed to determine solution independence and ensure resolution requirements are sufficient for capturing the combustion physics of interest. The combined effects of sudden expansion, high combustion temperatures, and wall-blown velocity result in a lower Reynolds number at the grain wall. Grain-wall resolution is set a priori based on the upstream inlet conditions and empirical resolution relationships determined in previous work [8]. Numerical simulations are performed on a coarse

and fine mesh, corresponding to 845k and 1.29M elements, respectively. Leveraging the polynomial adaptability of the DG formulation, numerical simulations are additionally performed with DG ($p = 0$), DG ($p = 1$), and DG ($p = 2$) elements on the fine mesh, resulting in 1, 3, and 6° of freedom per element, respectively. Table 10 summarizes the cases considered for the h and p refinement study. Cases are ordered based on the total degrees of freedom, showing the increased resolution as a result of both h and p refinement. The y^+ is calculated from the solution results based on the methodology of White [56]. To quantify the prediction error between the cases, a mean squared error, MSE, is defined:

$$\text{MSE} = \frac{\|\dot{r} - \dot{r}_T\|_{L2}}{\|\dot{r}_T\|_{L2}} \quad (31)$$

where \dot{r} is the predicted average regression rate of case i , \dot{r}_T is the baseline average regression rate predicted by the DG ($p = 2$) case, and $\|x\|_{L2}$ is an L2 norm operator. Previous work demonstrated that higher grid resolution is required to resolve diffusion flames using the reduced mechanisms in comparison to the skeletal mechanism [44]. As a consequence of reduced chemical pathways, there is a lack of fuel breakdown or slow oxidation reactions in the global mechanisms, resulting in a thinner heat release zone. The $h-p$ refinement study is performed using the two-step kinetics mechanism as a limiting case.

Figure 8 shows the instantaneous temperature comparison for the $h-p$ refinement study in the model SFRJ domain. There is

Table 10 Summary of cases considered for h and p refinement study with computed grid resolution and accuracy

Case	$\Delta h_{\min}, \mu\text{m}$	Elements	Degrees of freedom	y^+	MSE
Fine DG ($p = 0$)	35.0	1.29M	1.29M	3.29	3.77
Coarse DG ($p = 1$)	43.8	845k	2.54M	2.19	0.044
Fine DG ($p = 1$)	35.0	1.29M	3.87M	1.86	0.035
Fine DG ($p = 2$)	35.0	1.29M	7.74M	1.25	0.0

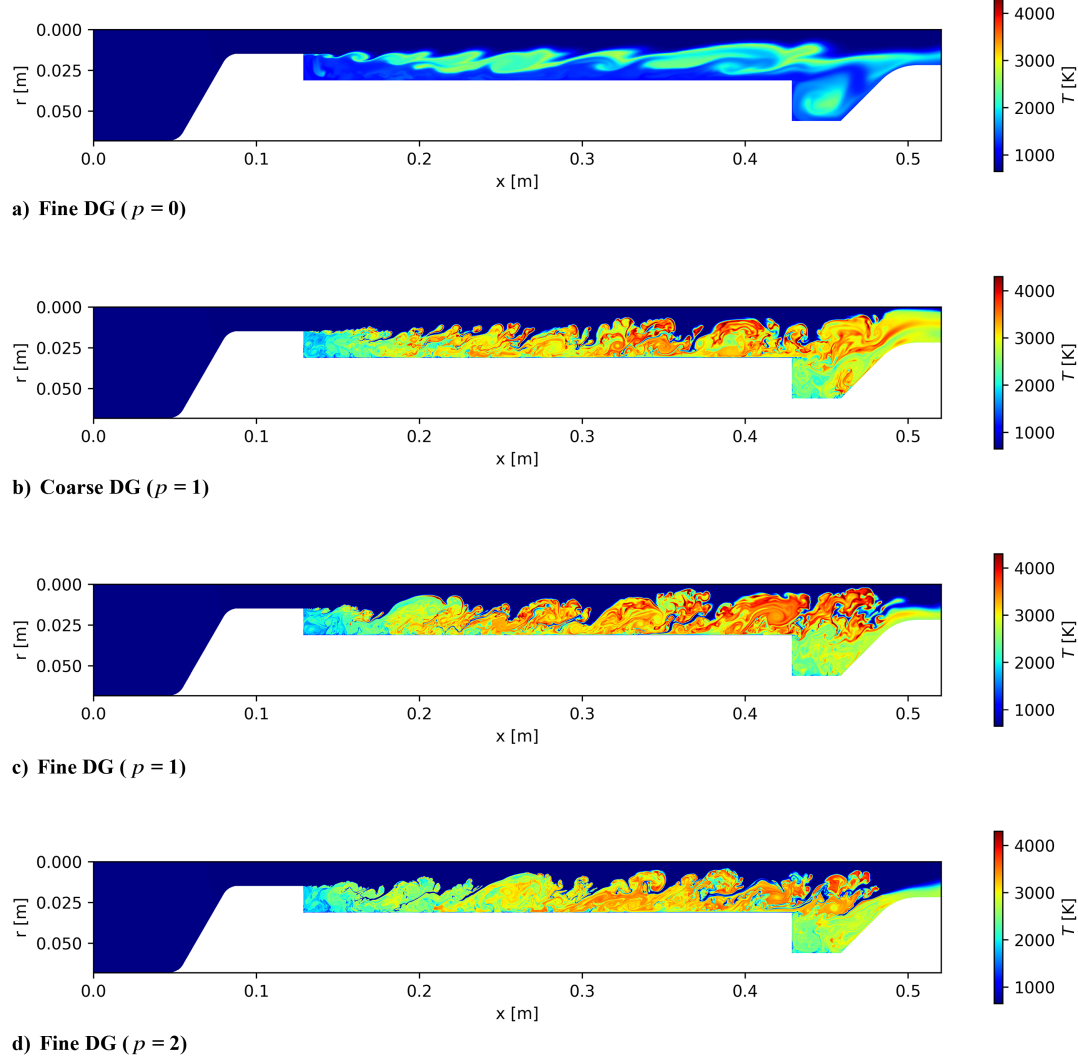


Fig. 8 Instantaneous temperature comparison for the $h-p$ refinement study in model SFRJ test case (simulations performed with the two-step kinetics mechanism).

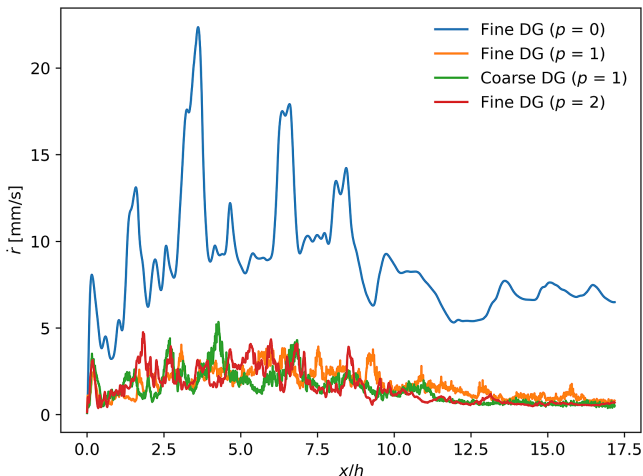


Fig. 9 Comparison of average axial regression rate with increasing p refinement in model SFRJ test case.

excellent agreement in the prediction of temperature and flame structure between the coarse DG ($p = 1$), fine DG ($p = 1$), and fine DG ($p = 2$) solutions. The temperature prediction within both the recirculation zones and cavity shows excellent agreement. The fine DG ($p = 0$) solution shows poor agreement with the rest of the cases, as the lack of resolution results in a very diffuse flame structure, leading to poor temperature prediction within the combustor.

Figure 9 shows the average predicted regression rate with increasing h and p refinement in the model SFRJ test case. Again, the coarse DG ($p = 1$), fine DG ($p = 1$), and fine DG ($p = 2$) solutions show excellent agreement, with the magnitude of MSE being 0.044 and 0.035 for the coarse DG ($p = 1$) and fine DG ($p = 1$), respectively. The fine DG ($p = 0$) simulation predicts the regression rate nearly 5 times larger than the other simulations, indicating that there is not adequate near wall-resolution to properly capture the pyrolysis physics. Excellent agreement between coarse DG ($p = 1$), fine DG ($p = 1$), and fine DG ($p = 2$) simulations indicates that the DG ($p = 1$) solution is sufficiently h - and p -refined to capture both the near wall and bulk the combustion physics. The fine mesh with DG ($p = 1$) elements is used for the duration of this work. The computed y^+ for the final six-step and skeletal mechanism cases are 1.32 and 1.19, respectively.

2. Temporal Convergence Study

A temporal convergence study is performed to verify the order of accuracy of the explicit 11-stage, 2nd-order strong stability-preserving Runge–Kutta time integration method [42]. Four numerical solutions are performed with fixed time steps Δt of $\Delta/2$, $\Delta/3$,

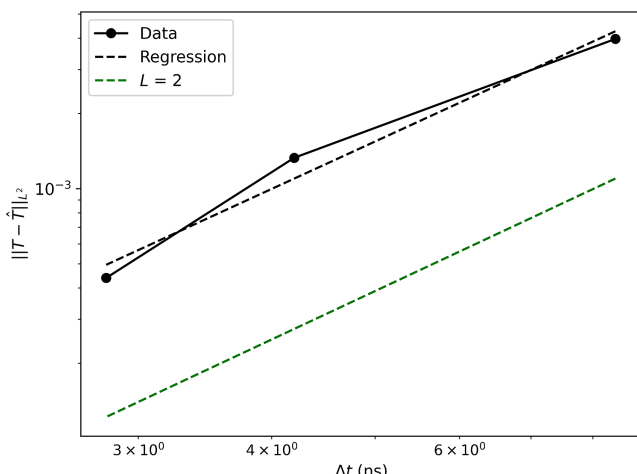


Fig. 10 Results of temporal convergence study. Expected order of accuracy, $L = 2$, plotted alongside for reference.

and $\Delta/4$, each run for a fixed interval of 100 Δ . An L2 norm of the centerline temperature at the end of the fixed interval with respect to the $\Delta t = \Delta/4$ case is taken. Figure 10 shows the results of the temporal convergence study, with the expected order of accuracy, $L = 2$, plotted alongside for reference. A linear regression is performed on the measured L2 norm error, measuring the order of accuracy to be 1.959 and confirming that the time integration scheme is second order.

D. Evaluation of Reaction Mechanisms in SFRJ Simulations

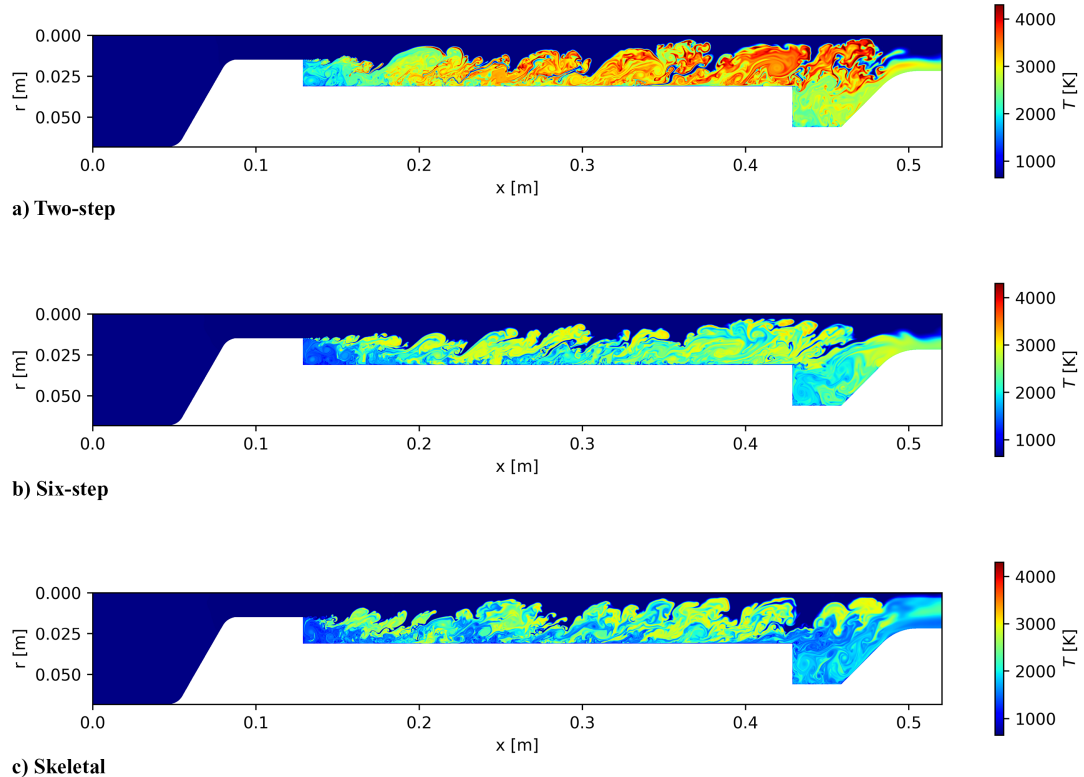
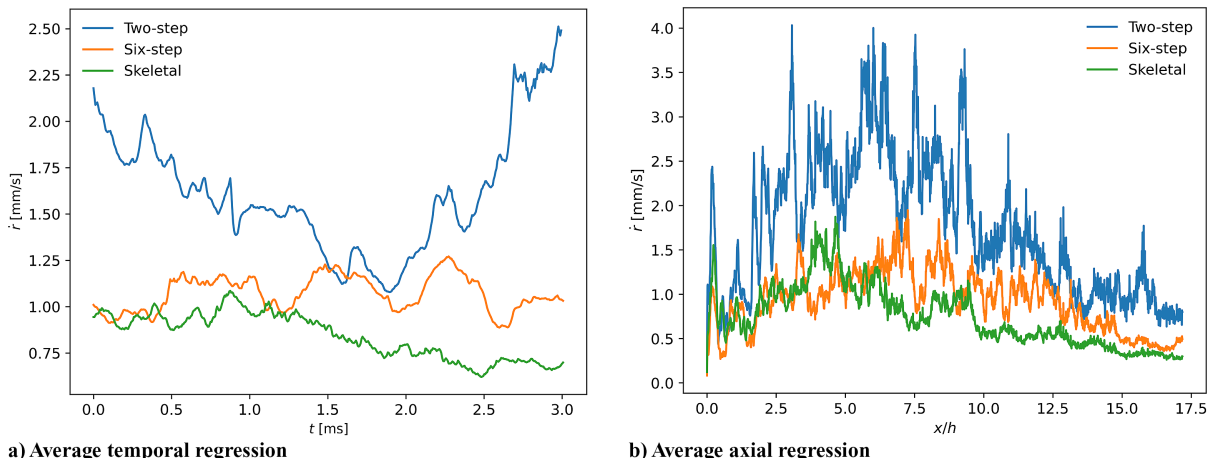
Solid-fuel ramjet simulations provide a more challenging and robust environment for testing the predictive capabilities of the reduced-order reaction mechanisms, necessitating accurate prediction in a partially premixed flame regime. Reduced mechanisms present a tradeoff between accuracy and speed of computation. Table 11 displays the normalized CPU cost for 1000 time steps for each mechanism performed on two AMD EPYC 7702 64-core processors. The normalized speedup metric shows that the two-step and six-step mechanisms are 10.249-times and 4.663-times faster compared to the skeletal mechanism, respectively. Additionally, memory requirements are reduced by 60 and 40% for the two- and six-step mechanisms, respectively, in comparison to the skeletal mechanism. Zero-dimensional calculations are performed with a time step of 1 ns to assess the acceleration ratio of chemical kinetics separate from species transport. The two-step and six-step mechanisms provide a 1.68-times and 1.32-times computational speedup in comparison to the skeletal mechanism, respectively, indicating that the vast majority of speedup is accomplished by reducing the number of transport equations. This improvement in cost allows for the scalability for larger and more computationally demanding problems, but at the expense of physical accuracy. The reduced mechanisms are compared to the skeletal mechanism to evaluate model performance for the prediction of key flame-marking scalars, flame structure, solid-fuel regression, and combustor efficiency.

Instantaneous flame temperature contours are displayed in Fig. 11. The two-step mechanism overpredicts the temperature considerably, with instantaneous temperatures reaching values higher than 4100 K for the duration of the simulation. This overprediction of temperature was also observed in earlier test configurations due to a lack of mitigating dissociation reactions and subsequent overprediction of specific heats [10]. The six-step and skeletal mechanisms show excellent agreement in instantaneous peak temperatures, with magnitudes between 3300 and 3400 K during the simulation run. The inclusion of dissociation reactions and alternative chemical pathways, which were absent in the two-step mechanism, regulates the peak temperature rise, leading to temperature magnitudes in agreement with the skeletal mechanism. The six-step mechanism is able to predict the temperature within the recirculation region with high accuracy; however, there is a discrepancy with the prediction of temperature in the aft-mixing end and temperature prediction near the wall in the downstream portion of the solid-fuel grain with the skeletal mechanism. This discrepancy can be partly attributed to the differing prediction of regression rate between the different mechanisms. Figure 12 shows the temporally and spatially resolved average regression rates predicted by the different reaction models. The two-step mechanism greatly overpredicts the average regression rate, while the six-step and skeletal mechanisms show agreement within the same order of accuracy. On average, the six-step mechanism slightly overpredicts the regression rate in comparison to the skeletal mechanism, releasing more fuel into the domain. Spatially, the disagreement in regression rate magnitude is largely constrained to the downstream portion of the fuel grain, resulting in a larger amount of unburnt fuel advecting downstream to the aft-mixing region.

To quantify the predictions between the reduced mechanism and skeletal mechanisms, a 95% confidence interval of the average regression rate is constructed, and a mean squared error, MSE, is calculated using the average axial regression rate of the skeletal mechanism as a baseline. Table 12 displays the quantified regression rate prediction between the reaction mechanisms. The 95% confidence interval of the

Table 11 Normalized comparison of CPU cost (1 node and 1000 time steps)

Mechanism	Total time, s	Time per step, s	Throughput, cell/s	Normalized speedup
2-Step	1.2617e + 03	1.2617	1.0205e + 06	10.249
6-Step	2.7734e + 03	2.7734	4.6425e + 05	4.663
Skeletal	1.2931e + 04	12.931	9.9572e + 04	1.000

**Fig. 11** Instantaneous temperature comparison by reaction mechanism in SFRJ test case.**a) Average temporal regression****b) Average axial regression****Fig. 12** Simulated regression rate comparison for SFRJ test case.**Table 12** Quantification of regression rate prediction by mechanism for SFRJ test case

Mechanism	95% CI, mm/s	MSE
2-Step	[1.4262,1.8008]	2.017
6-Step	[0.8858,1.2604]	0.204
Skeletal	[0.6556,1.0302]	0.0

true regression rate shows significant overlap between the six-step and skeletal mechanisms. The two-step again significantly overpredicts the regression rate in comparison to both the six-step and skeletal mechanisms, with a confidence interval that doesn't overlap either mechanism. The MSE, calculated based on the skeletal mechanism, shows an order of magnitude better agreement between the six-step mechanism as compared to the two-step mechanism. Improved prediction of temperature by the six-step mechanism directly improves regression rate prediction.

Figures 13–15 show instantaneous Y_{CO_2} , $Y_{\text{H}_2\text{O}}$, and $Y_{\text{C}_4\text{H}_6}$ contour comparisons by reaction mechanism, respectively. As expected, the two-step mechanism overpredicts both Y_{CO_2} and $Y_{\text{H}_2\text{O}}$ compared to the skeletal mechanism, contributing to the overprediction of

temperature. Due to the singular fuel breakdown pathways for C_4H_6 in (R1), the overprediction of $Y_{\text{H}_2\text{O}}$ cannot be mitigated. The magnitude of Y_{CO_2} within the recirculation region is reasonable but continues to increase axially along the length of the combustor.

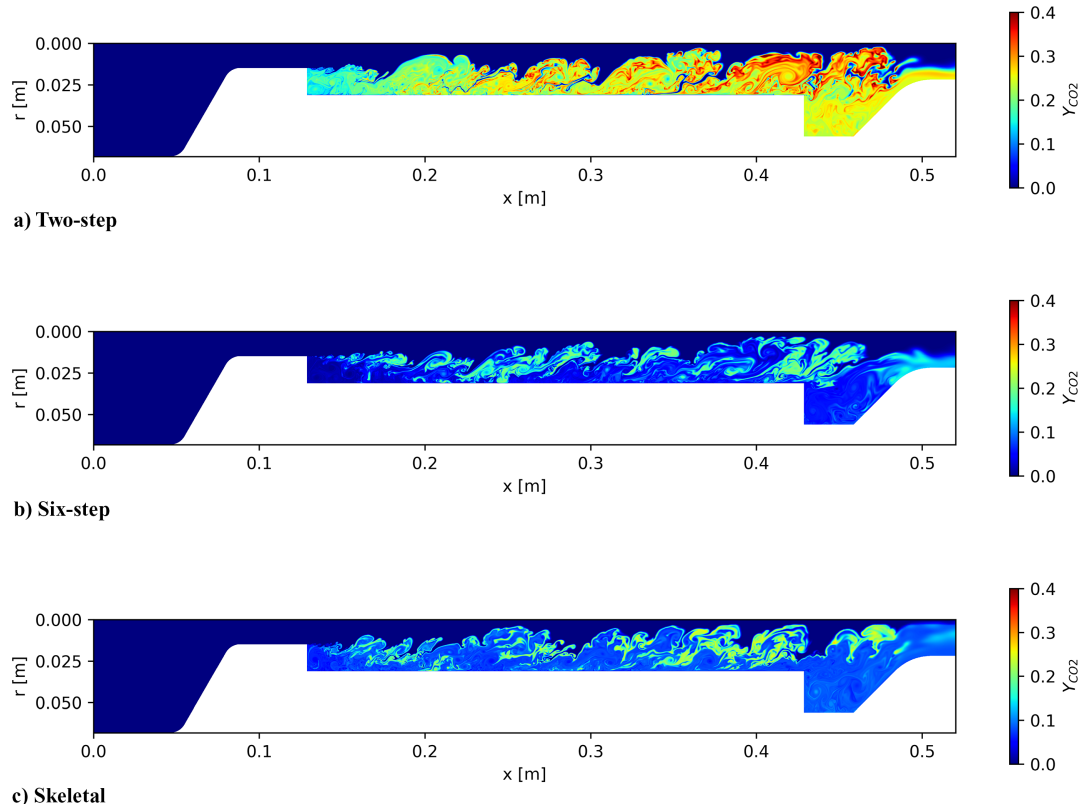


Fig. 13 Instantaneous Y_{CO_2} comparison by reaction mechanism in SFRJ test case.

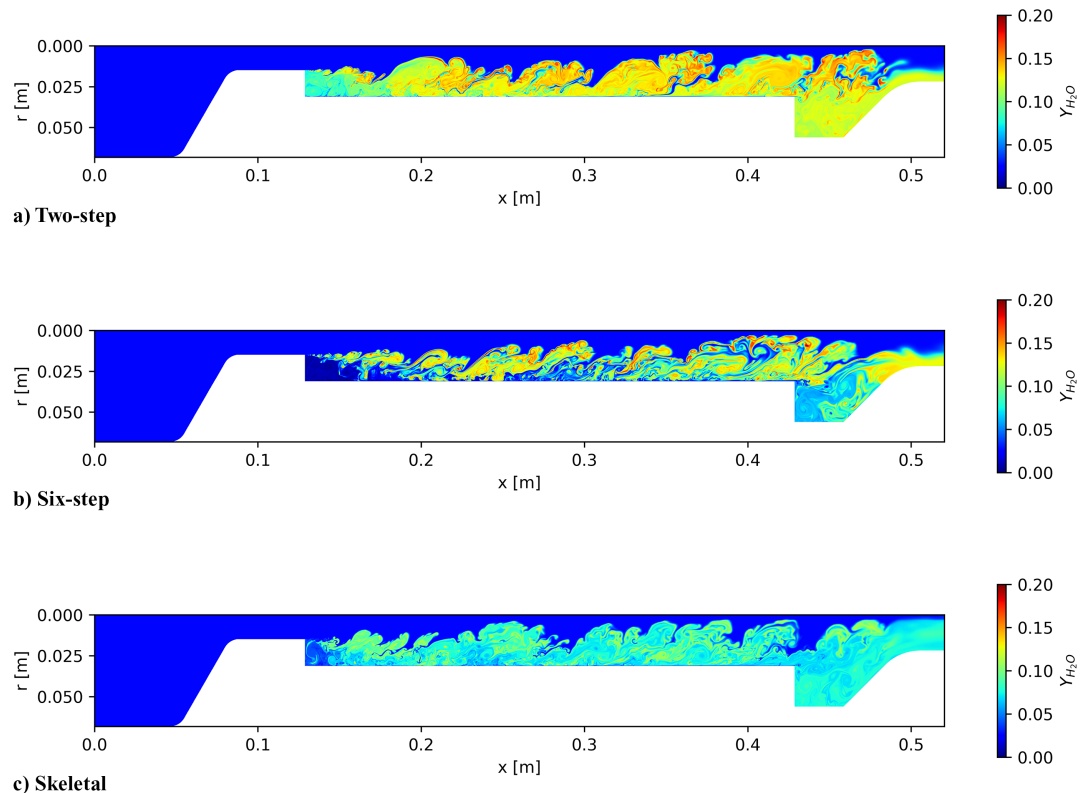


Fig. 14 Instantaneous $Y_{\text{H}_2\text{O}}$ comparison by reaction mechanism in SFRJ test case.

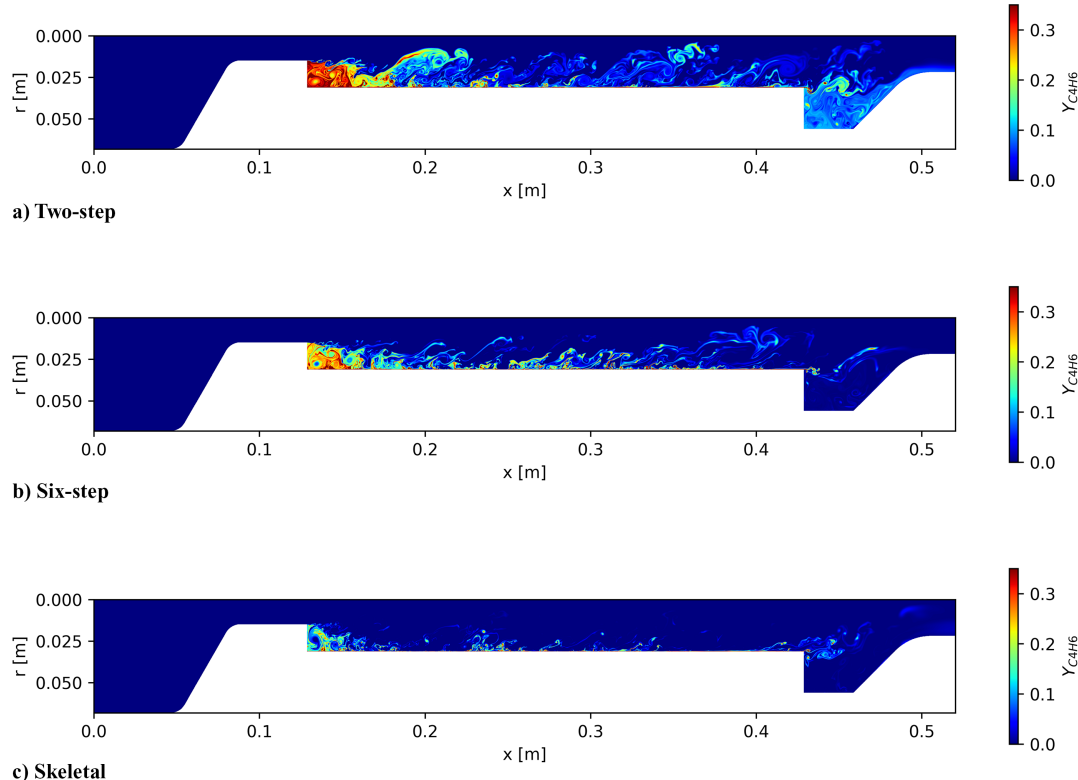


Fig. 15 Instantaneous $Y_{C_4H_6}$ comparison by reaction mechanism in SFRJ test case.

With limitations in chemical pathways resulting in artificially high specific heats, there is an increase in temperature that results in an artificially high regression rate. As the mixture becomes richer due to higher amounts of C_4H_6 present, there is an increased rate of CO to CO_2 oxidation, which compounds the issue. In comparison, the six-step mechanism shows improved agreement with the skeletal mechanism in the prediction of instantaneous Y_{CO_2} and Y_{H_2O} mass fractions. The magnitude of Y_{CO_2} shows very good agreement, while the magnitude of Y_{H_2O} shows reasonable agreement with the skeletal mechanism. For both global reaction mechanisms, the magnitude of $Y_{C_4H_6}$ within the combustor is significantly higher than the skeletal mechanism. This can again be explained by the lack of fuel breakdown pathways, as C_4H_6 is quickly broken down into smaller hydrocarbon species within the skeletal mechanism, mainly C_2H_2 , C_2H_3 , and C_2H_4 . Overall, species prediction in the six-step mechanism is significantly improved in comparison to the two-step mechanism. Particularly, with the inclusion of important dissociation reactions leading to more reasonable predictions of major species.

A major calibration target for the reduced global mechanisms is the prediction of flame thickness, important for accurate prediction of unsteady flame dynamics. A comparison of the instantaneous vorticity contours, ζ_θ , for the different reaction mechanisms is shown in Fig. 16. The magnitude and distribution of vorticity across all the mechanisms show good qualitative agreement, indicating the reduced mechanisms ability to reproduce similar features of unsteady flame dynamics, which are important to the mixing, burning, and convective heat transfer to the solid-fuel surface. In order to further quantify the prediction of unsteady flame dynamics, a flame edge detection algorithm is employed. Figure 17 shows the leading flame edge detected for a representative instantaneous temperature contour, with the flame edge denoted by Ψ . The leading flame edge is detected for each instantaneous sample at the extreme $T = 800$ K isotherm. A probability density function (PDF) of flame edge, $PDF(\Psi)$, is constructed at each axial location, where the probability of finding the flame edge within a given radius at an axial station is given by

$$p(\Psi \in [r_a, r_b]) = \int_{r_a}^{r_b} PDF(\Psi) dr \quad (32)$$

The result is compiled in Fig. 18, which shows the local axial PDF of the flame edge compiled along the length of the SFRJ combustor. The PDF essentially resolves the flame brush of the leading edge of the flame, which gives insight into the prediction of unsteady flame dynamics. The two-step and six-step mechanism demonstrate agreement with the flame brush predicted by the skeletal mechanisms downstream of $x/h = 5.0$. The six-step mechanism shows improved agreement with the skeletal mechanism in representing the overall width of the flame brush, while the two-step mechanism shows better agreement in capturing the flame brush slope with respect to downstream direction as compared with the skeletal mechanism. The deviations in the flame brush can be attributed to the poor agreement upstream at $x/h < 5$. The skeletal mechanism shows a much wider distribution of leading flame edge near the backward-facing step lip, whereas the reduced mechanisms show a thinner distribution of leading flame edge. For the skeletal mechanism, there is a significant flame standoff that varies with time during the simulation run. This flame standoff is correlated to the ignition delay time; i.e., the time required for C_4H_6 to breakdown and for chain-branching reactions to begin. This chemistry is nonexistent in the reduced mechanisms, which are unable to reproduce this trend. To visualize this effect further, a slice is taken at $x/h = 1$ and the average and standard deviation of the temperature are plotted in Fig. 19. For the two-step and six-step mechanisms, there is a sharp increase in temperature due to the flame anchoring directly off the backward-facing step, contrasted to the skeletal mechanism that has a gradual temperature rise due to the increased flame standoff from the backward-facing step. The six-step mechanism is able to reproduce the average temperature within the recirculation zone with high accuracy in comparison to the skeletal mechanism, but the flame edge and progress of reactions are not well predicted. The two-step mechanism overpredicts the temperature within the recirculation zone drastically, leading to larger

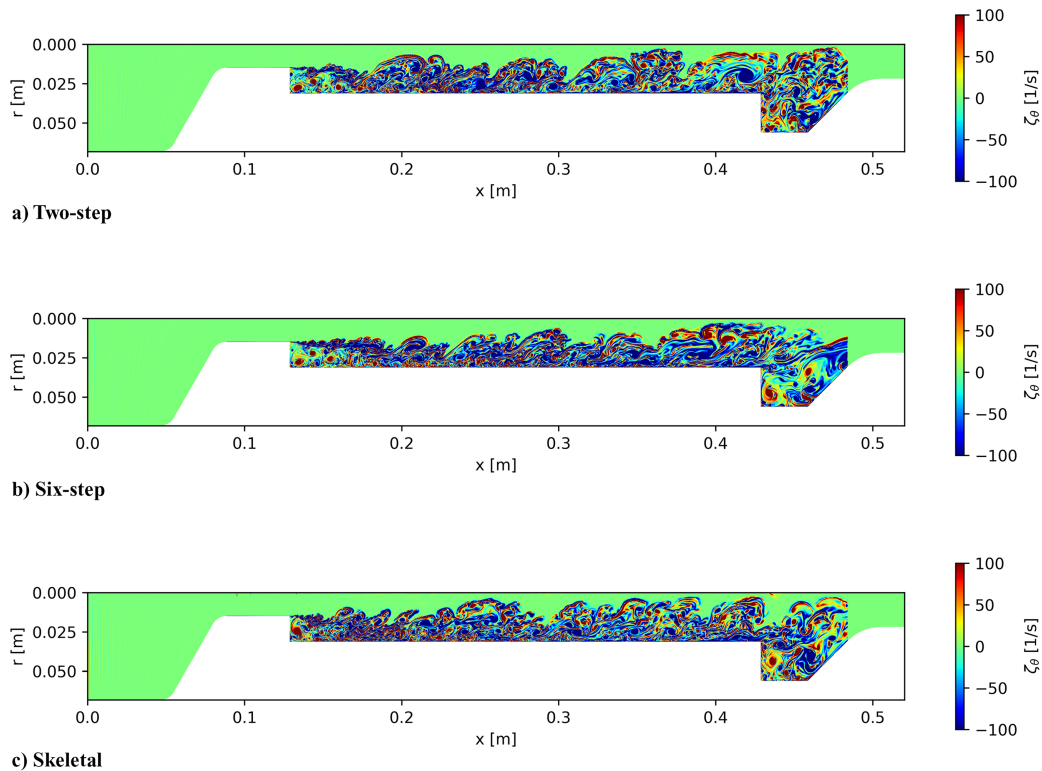


Fig. 16 Instantaneous vorticity comparison by reaction mechanism in SFRJ test case.

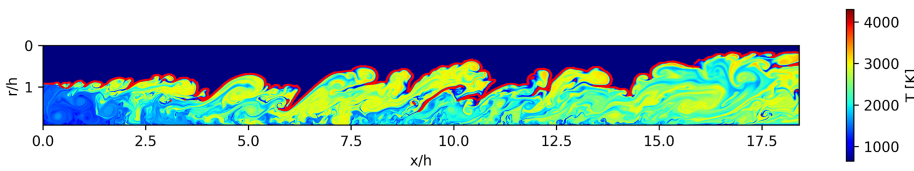


Fig. 17 Flame edge detection (Ψ colored red).

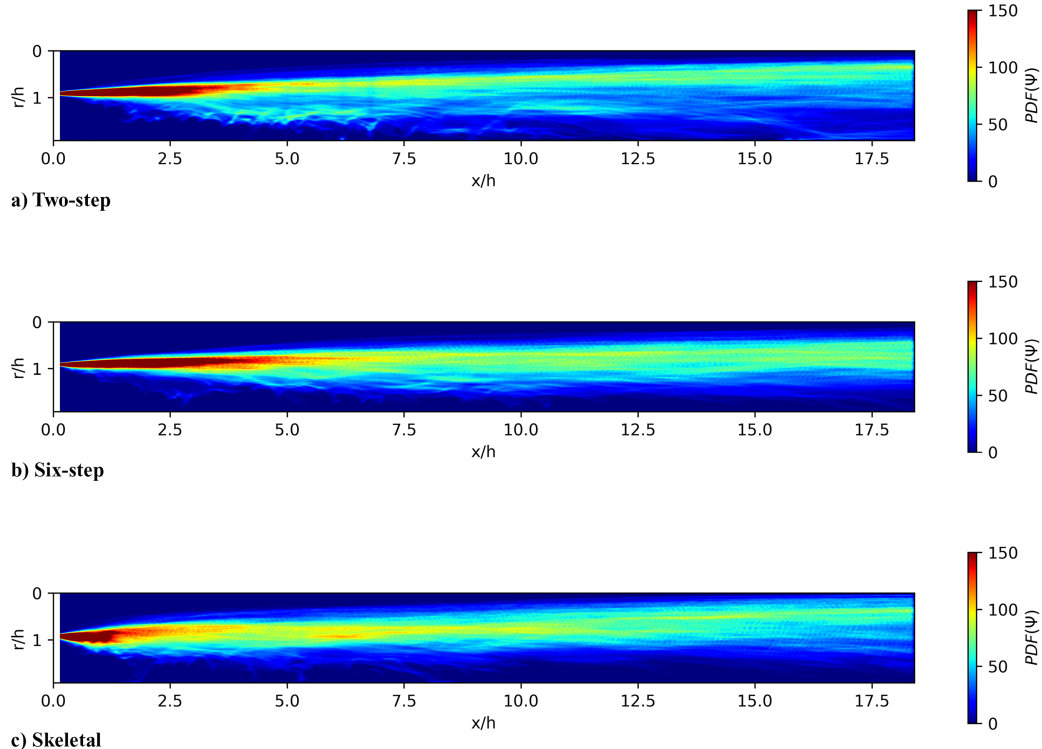


Fig. 18 PDF of flame edge comparison in SFRJ test case.

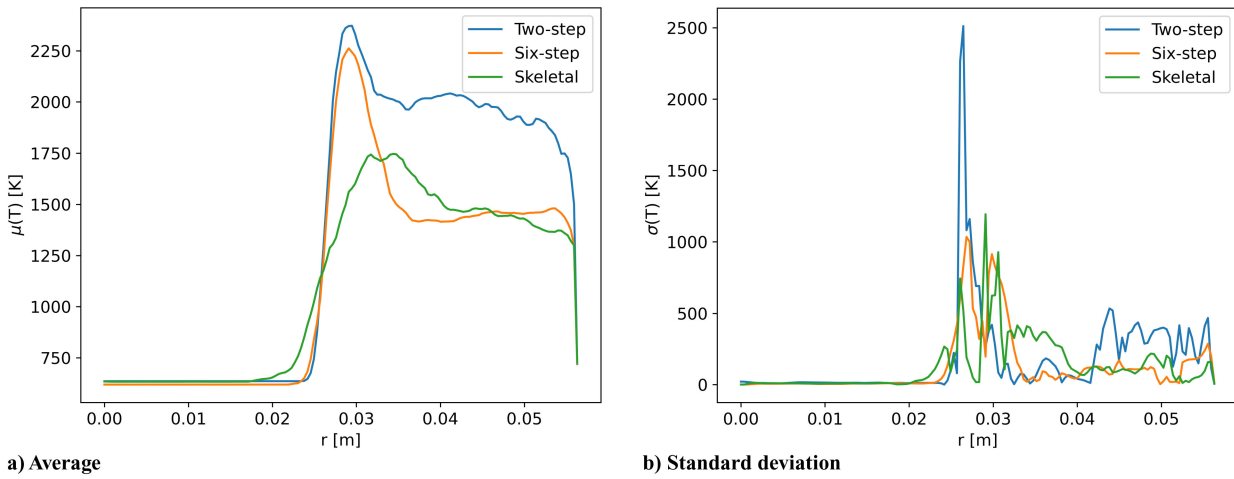


Fig. 19 Temperature slice in recirculation region comparison for SFRJ test case.

gradients in temperature at the wall. The temperature and flame edge PDF shows that the skeletal mechanism predicts higher protrusion of the unsteady flame into the freestream, as evidenced by the higher average temperature at $r = 0.02$ m and wider PDF. The two-step mechanism has the highest standard deviation; as a consequence, it has a higher magnitude temperature prediction and a thinner heat release zone. The six-step and skeletal mechanisms show improved agreement in the magnitude of temperature standard deviation in the shear layer and in the recirculation zone, indicating that the unsteady combustion dynamics are better captured by the six-step mechanism. This agrees with the better prediction of flame brush width by the six-step mechanism, indicating that more accurate temperature prediction leads to better prediction of unsteady flame effects.

The reduced mechanisms are able to reasonably predict the unsteady flame dynamics, evidenced by similarities in the predicted flame brush and instantaneous vorticity. However, the reduced mechanisms are not capable of capturing some of the salient features of SFRJ flame-holding due to limitations in the available chemical pathways. Another challenging metric for the global mechanisms is in the prediction of engine efficiency. For SFRJ engines, the characteristic velocity c^* is commonly employed to evaluate engine performance, defined as

$$c^* = \frac{C_D p_4 A_t}{\dot{m}_T} \quad (33)$$

where C_D is the discharge coefficient of the nozzle, estimated to be 0.9, p_4 is the average pressure at the aft-end of the mixing chamber, and \dot{m}_T is the total mass flow rate leaving the engine. This is the main metric used to evaluate the combustor performance in the experimental firing of the model SFRJ engine [54]. The c^* efficiency is challenging for reduced models to match, requiring accurate prediction of thermal efficiency and regression rate. Figure 20 shows the simulated c^* efficiency comparison by mechanism for the SFRJ test case. Immediately, it can be seen that both mechanisms show similar fluctuations in c^* efficiency in comparison to the skeletal mechanism. This suggests that the mechanisms are able to predict fluctuations due to unsteady combustion dynamics. Table 13 displays the average c^* efficiency, \bar{c}^* , for the reduced mechanisms, skeletal mechanism, and experiment. There is a monotonic increase in accuracy with increasing kinetics model fidelity, with the skeletal mechanism converging almost exactly on the experimental c^* efficiency. The six-step mechanism shows great agreement with 5% of the experimental value, while the two-step mechanism shows predicted c^* above 11%. The overprediction by the two-step mechanism is largely driven by the increased combustion temperature and associated pressure rise. However, all the mechanisms show good agreement with the experimental c^* efficiency, demonstrating their ability to reproduce experimental trends.

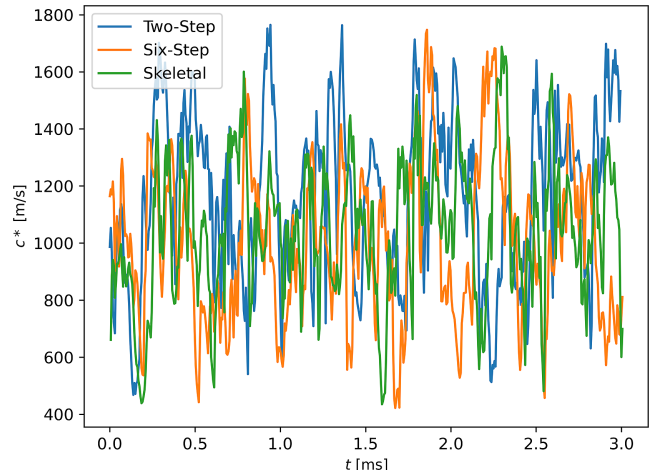


Fig. 20 Simulated c^* efficiency comparison for SFRJ test case.

Table 13 Average c^* comparison by mechanism with experiment

Methodology	\bar{c}^* , m/s	Percent difference, %
2-Step	1167.6	11.2
6-Step	1000.3	4.73
Skeletal	1045.9	0.39
Experimental	1050	0.0

Efficient numerical simulations of HTPB–air combustion within SFRJ engines are demonstrated with varying levels of accuracy using the reduced global mechanisms, prompting comparison analysis for future engine design. The two-step mechanism provides the largest cost reduction and reasonable prediction of overall combustor c^* efficiency; however, the two-step mechanism is unable to faithfully reproduce temperature, regression rate, or species concentrations. The six-step mechanism requires roughly twice the numerical cost in comparison to the two-step mechanism but provides superior prediction of combustor efficiency, regression rate, and instantaneous temperature. Faithful reproduction of species, inclusion of intermediates, and insight into combustor flame-holding require the use of models with higher fidelity than global reduced models. These models provide practical utility throughout the design process of new SFRJ engines, with the two-step mechanism capable of providing quick geometric screening during early design and the six-step mechanism providing robust regression rate and performance metrics for detailed design.

V. Conclusions

Robust reduced-order 1,3-butadiene kinetics mechanisms are required for efficient numerical simulations of HTPB–air combustion within SFRJ engines. Starting from initial models calibrated for HRE applications with 100% oxygen, this study describes the development and evaluation of two-step and six-step finite-rate chemistry mechanisms for 1,3-butadiene combustion in air intended for modeling SFRJ engines. A sensitivity study based on the extinction strain rate of strained counterflow diffusion flames is performed. The pre-exponential factor for the Arrhenius rate expressions is calibrated in order to reproduce the prediction of extinction strain rate and temperature.

Evaluation of the calibrated reduced-order models is performed on a series of zero-, one-, and two-dimensional numerical simulations. A high-fidelity 20-species, 109-reaction pressure comprehensive skeletal kinetics mechanism serves as a baseline for all simulations. Zero-dimensional equilibrium calculations show that the two-step mechanism is unable to properly predict equilibrium temperature and composition, limiting the utility of this mechanism in the prediction of combustion dynamics. The inclusion of radical species in the six-step mechanism leads to accurate modulation of the equilibrium flame temperature and composition. One-dimensional solid-fuel counterflow diffusion flames are modeled in CANtera with a fully coupled solid-fuel pyrolysis boundary condition. Both tailored reduced mechanisms show good agreement with the skeletal mechanism in the prediction of regression rate, flame temperature, and flame thickness with increasing pressure. The six-step mechanism predicts a higher maximum flame temperature in comparison to baseline solutions but provides improved regression rate prediction over the two-step mechanism in one-dimensional counterflow flames.

Two-dimensional axisymmetric LES simulations of an SFRJ combustor are performed using a fully coupled solid-fuel pyrolysis boundary condition. The $h-p$ refinement and temporal convergence studies are performed to establish grid independence and order of accuracy of the numerical scheme. Results show the two-step mechanism overpredicting the temperature drastically, leading to an overprediction of regression rate. The six-step mechanism shows good agreement in the prediction of temperature and regression rate in comparison to the skeletal mechanism due to the inclusion of dissociation reactions. Further, the six-step mechanism shows significant improvement in the two-step mechanism in the prediction of species mass fractions and overall c^* efficiency. Both mechanisms provide a meaningful computational speedup in comparison to the skeletal mechanism, but the lack of available chemical pathways by both reduced reaction mechanisms limits their utility in capturing features of the combustion physics. The reduced mechanisms overpredict the amount of 1,3-butadiene within the flowfield and are unable to capture features of flame-anchoring, as there are no endothermic fuel breakdown pathways. Given proper consideration of the limitations inherent, the reduced mechanisms provide accurate scale-resolved SFRJ simulations with significant reductions in computational expense.

Appendix: Laminar Flame Speed Sensitivities

Figure A1 displays the results of the brute-force sensitivity analysis of freely propagating laminar flames at $T = 300$ K and $P = 1$ atm, with a variable equivalence ratio between $\phi = 0.6$ and $\phi = 1.4$ to explore both mechanism performances in fuel-lean, stoichiometric, and fuel-rich combustion conditions. The flame speed is dominated by (R1) for the two-step reaction across all equivalence ratios, from fuel-lean to fuel-rich. Reactions (R1) and

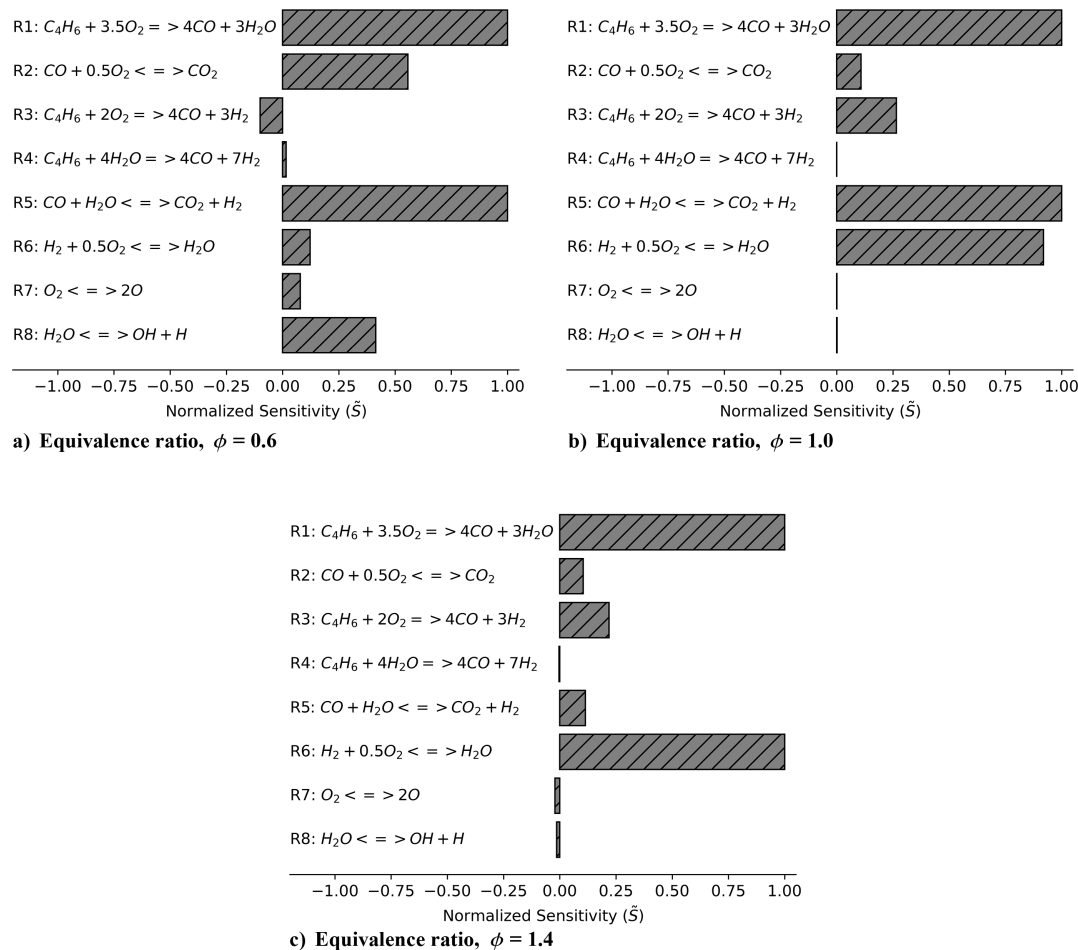


Fig. A1 Brute-force sensitivity analysis of two-step and six-step 1,3-butadiene flame speed at $T = 300$ K, $P = 1$ atm, and equivalence ratio $\phi = 0.6, 1.0, 1.4$.

(R2) compete for oxygen consumption, and a greater amount of heat release of 1,3-butadiene is controlled by (R1), resulting in greater sensitivity. The sensitivity of (R2) decreases significantly with increased equivalence ratio as the limited amount of oxygen is consumed primarily by (R1) and results in much greater flame speeds. The laminar flame speed for the six-step reaction mechanism is dominated by reactions (R5) and (R6). Again, in fuel-lean conditions the oxidation of CO to CO₂ plays a more critical role in heat release compared to in fuel-rich conditions, where the oxidation of H₂ to H₂O plays a more critical role in heat release. Thus, as the equivalence ratio increases, the water-phase shift (R5), which favors CO oxidation, loses prominence in favor for the H₂ oxidation supplied by (R6). At the stoichiometric equivalence ratio, the laminar flame speed is nearly equal in sensitivity between reactions (R5) and (R6), which compete to produce CO₂ and H₂O, respectively.

Acknowledgments

This work was sponsored by the Office of Naval Research through the NRL 6.1 Base Program and the Hypersonic Aerothermodynamics, High-Speed Propulsion and Materials portfolio (PM: Dr. Eric Marineau). Computing resources were generously provided by the Department of Defense High Performance Computing Modernization Program. Ryan DeBoskey was supported through the National Defense Science and Engineering Graduate (NDSEG) Fellowship. The authors would like to acknowledge Dr. Andrew Corrigan for assistance provided with the overall computational framework of the JENRE® Multiphysics Framework.

References

- [1] Ajaz, A., "Hydroxyl-Terminated Polybutadiene Telechelic Polymer (HTPB): Binder for Solid Rocket Propellants," *Rubber Chemistry and Technology*, Vol. 68, No. 3, 1995, pp. 481–506. <https://doi.org/10.5254/1.3538752>
- [2] Dennis, C., and Bojko, B., "On the Combustion of Heterogeneous AP/HTPB Composite Propellants: A Review," *Fuel*, Vol. 254, Oct. 2019, Paper 115646. <https://doi.org/10.1016/j.fuel.2019.115646>
- [3] George, P., Krishnan, S., Varkey, P., Ravindran, M., and Ramachandran, L., "Fuel Regression Rate in Hydroxyl-Terminated-Polybutadiene/Gaseous-Oxygen Hybrid Rocket Motors," *Journal of Propulsion and Power*, Vol. 17, No. 1, 2001, pp. 35–42. <https://doi.org/10.2514/2.5704>
- [4] Krishnan, S., and George, P., "Solid Fuel Ramjet Combustor Design," *Progress in Aerospace Sciences*, Vol. 34, Nos. 3–4, 1998, pp. 219–256. [https://doi.org/10.1016/S0376-0421\(98\)00005-0](https://doi.org/10.1016/S0376-0421(98)00005-0)
- [5] Schulte, G., "Fuel Regression and Flame Stabilization Studies of Solid-Fuel Ramjets," *Journal of Propulsion and Power*, Vol. 2, No. 4, 1986, pp. 301–304. <https://doi.org/10.2514/3.22886>
- [6] Gallegos, D., Pace, H., Arnold, C., Massa, L., and Young, G., "Regression and Flame Structure in Cavity Flameholding Solid-Fuel Ramjet Fuel Grains," *Journal of Propulsion and Power*, Vol. 39, No. 6, 2023, pp. 1–11. <https://doi.org/10.2514/1.B39139>
- [7] Musa, O., Xiong, C., Chang-sheng, Z., Ying-kun, L., and Wen-He, L., "Investigations on the Influence of Swirl Intensity on Solid-Fuel Ramjet Engine," *Computers and Fluids*, Vol. 167, May 2018, pp. 82–99. <https://doi.org/10.1016/j.compfluid.2018.02.033>
- [8] DeBoskey, R. D., Kessler, D. A., Patel, T. K., Bojko, B. T., Johnson, R., Goodwin, G. B., Narayanaswamy, V., and Hess, A., "Analysis of Flame Structures in a Model Solid Fuel Ramjet Combustor with Increasing Reynold's Number," AIAA Paper 2024-2595, Jan. 2024. <https://doi.org/10.2514/6.2024-2595>
- [9] Whitmore, S. A., Peterson, Z. W., and Eilers, S. D., "Comparing Hydroxyl Terminated Polybutadiene and Acrylonitrile Butadiene Styrene as Hybrid Rocket Fuels," *Journal of Propulsion and Power*, Vol. 29, No. 3, 2013, pp. 582–592. <https://doi.org/10.2514/1.B34382>
- [10] Morinigo, J., and Hermida-Quesada, J., "Evaluation of Reduced-Order Kinetics Models for HTPB-Oxygen Combustion Using LES," *Aerospace Science and Technology*, Vol. 58, Nov. 2016, pp. 358–368. <https://doi.org/10.1016/j.ast.2016.08.027>
- [11] Panchal, A., and Menon, S., "Modeling the Effect of Metal Particles on Solid Fuel Burning in a Ramjet Combustor," AIAA Paper 2024-1413, Jan. 2024. <https://doi.org/10.2514/6.2024-1413>
- [12] Kalman, J., Guerra, A. S., Karapetian, J., Patnala, M. S. S. M., and Kastengren, A. L., "Surface Structure of Reacting Solid Ramjet Fuels," *Journal of Propulsion and Power*, Vol. 40, No. 3, 2024, pp. 411–419. <https://doi.org/10.2514/1.B39281>
- [13] Arisawa, H., and Brill, T. B., "Flash Pyrolysis of Hydroxyl-Terminated Polybutadiene (HTPB) I: Analysis and Implications of the Gaseous Products," *Combustion and Flame*, Vol. 106, Nos. 1–2, 1996, pp. 131–143. [https://doi.org/10.1016/0010-2180\(96\)00253-2](https://doi.org/10.1016/0010-2180(96)00253-2)
- [14] Chiaverini, M. J., Harting, G. C., Lu, Y. C., Kuo, K. K., Peretz, A., Jones, H. S., Wygle, B. S., and Arves, J. P., "Pyrolysis Behavior of Hybrid-Rocket Solid Fuels Under Rapid Heating Conditions," *Journal of Propulsion and Power*, Vol. 15, No. 6, 1999, pp. 888–895. <https://doi.org/10.2514/2.5512>
- [15] Bojko, B. T., Gross, M. L., and Jackson, T. L., "Investigating Dimensional Effects on Predicting Burning Rates of Heterogeneous Solid Propellants," *AIAA Journal*, Vol. 58, No. 4, 2020, pp. 1724–1732. <https://doi.org/10.2514/1.J058631>
- [16] Gross, M., and Beckstead, M., "Diffusion Flame Calculations for Composite Propellants Predicting Particle-Size Effects," *Combustion and Flame*, Vol. 157, No. 5, 2010, pp. 864–873. <https://doi.org/10.1016/j.combustflame.2009.09.004>
- [17] Ganesh, K., Sundarrajan, S., Kishore, K., Ninan, K. N., George, B., and Surianarayanan, M., "Primary Pyrolysis Products of Hydroxyl-Terminated Polybutadiene," *Macromolecules*, Vol. 33, No. 2, 2000, pp. 326–330. <https://doi.org/10.1021/ma990423p>
- [18] Laskin, A., Wang, H., and Law, C. K., "Detailed Kinetic Modeling of 1, 3-Butadiene Oxidation at High Temperatures," *International Journal of Chemical Kinetics*, Vol. 32, No. 10, 2000, pp. 589–589. [https://doi.org/10.1002/1097-4601\(2000\)32:103.0.CO;2-U](https://doi.org/10.1002/1097-4601(2000)32:103.0.CO;2-U)
- [19] Zhou, C. W., Li, Y., Burke, U., Banyon, C., Somers, K. P., Ding, S., Khan, S., Hargis, J. W., Sikes, T., and Mathieu, O., et al., "An Experimental and Chemical Kinetic Modeling Study of 1,3-Butadiene Combustion: Ignition Delay Time and Laminar Flame Speed Measurements," *Combustion and Flame*, Vol. 197, Nov. 2018, pp. 423–438. <https://doi.org/10.1016/j.combustflame.2018.08.006>
- [20] Wang, H., Dames, E., Sirjean, B., Sheen, D. A., Tango, R., Violi, A., Lai, J. Y. W., Egolfopoulos, F. N., Davidson, D. F., Hanson, R. K., et al., "A High-Temperature Chemical Kinetic Model of n-Alkane (up to n-Dodecane), Cyclohexane, and Methyl-, Ethyl-, n-Propyl and n-Butyl-Cyclohexane Oxidation at High Temperatures," JetSurF Ver. 2.0, Sept. 2010, <http://web.stanford.edu/group/haiwanglab/JetSurF/JetSurF2.0/index.html>
- [21] Curran, H. J., "Developing Detailed Chemical Kinetic Mechanisms for Fuel Combustion," *Proceedings of the Combustion Institute*, Vol. 37, No. 1, 2019, pp. 57–81. <https://doi.org/10.1016/j.proci.2018.06.054>
- [22] Sankaran, V., "Computational Fluid Dynamics Modeling of Hybrid Rocket Flowfields," *Progress in Astronautics and Aeronautics*, Vol. 218, 2007, pp. 323–349.
- [23] Frassoldati, A., Cuoci, A., Faravelli, T., Ranzi, E., Candusso, C., and Tolazzi, D., "Simplified Kinetic Schemes for Oxy-Fuel Combustion," *Proceedings of the 1st International Conference on Sustainable Fossil Fuels for Future Energy, CO2Club*, Carbonia, Italy, 2009, pp. 6–10.
- [24] Gariani, G., Maggi, F., and Galfetti, L., "Numerical Simulation of HTPB Combustion in a 2D Hybrid Slab Combustor," *Acta Astronautica*, Vol. 69, No. 5–6, 2011, pp. 289–296. <https://doi.org/10.1016/j.actaastro.2011.03.015>
- [25] Morínigo, J. A., and Hermida-Quesada, J., "Evaluation of Reduced-Order Kinetic Models for HTPB-Oxygen Combustion Using LES," *Aerospace Science and Technology*, Vol. 58, Nov. 2016, pp. 358–368. <https://doi.org/10.1016/j.ast.2016.08.027>
- [26] Gong, L., Chen, X., Musa, O., Yang, H., and Zhou, C., "Numerical and Experimental Investigation of the Effect of Geometry on Combustion Characteristics of Solid-Fuel Ramjet," *Acta Astronautica*, Vol. 141, Dec. 2017, pp. 110–122. <https://doi.org/10.1016/j.actaastro.2017.09.027>
- [27] Bojko, B. T., Patel, T. K., Kessler, D. A., and DeBoskey, R. D., "Investigating the Reacting Flow-Field Within a Model Solid Fuel Ramjet Combustor Using the Flamelet Progress Variable Approach," AIAA Paper 2024-1415, Jan. 2024. <https://doi.org/10.2514/6.2024-1415>
- [28] Westbrook, C. K., and Dryer, F. L., "Simplified Reaction Mechanisms for the Oxidation of Hydrocarbon Fuels in Flames," *Combustion*

- Science and Technology*, Vol. 27, No. 1–2, 1981, pp. 31–43.
<https://doi.org/10.1080/00102208108946970>
- [29] Jones, W. P., and Lindstedt, R. P., “Global Reaction Schemes for Hydrocarbon Combustion,” *Combustion and Flame*, Vol. 73, No. 3, 1988, pp. 233–249.
[https://doi.org/10.1016/0010-2180\(88\)90021-1](https://doi.org/10.1016/0010-2180(88)90021-1)
- [30] McBride, B. J., Gordon, S., and Reno, M. A., “Coefficients for Calculating Thermodynamic and Transport Properties of Individual Species,” NASA Glenn Research Center, NASA TM 4513, 1993.
- [31] McBride, B. J., Zehe, M. J., and Gordon, S., “NASA Glenn Coefficients for Calculating Thermodynamic Properties of Individual Species,” NASA Glenn Research Center, NASA TP 2002-211556, 2002.
- [32] Coffee, T., and Heimerl, J., “Transport Algorithms for Premixed, Laminar Steady-State Flames,” *Combustion and Flame*, Vol. 43, 1981, pp. 273–289.
[https://doi.org/10.1016/0010-2180\(81\)90027-4](https://doi.org/10.1016/0010-2180(81)90027-4)
- [33] Houim, R., and Kuo, K., “A Low-Dissipation and Time-Accurate Method for Compressible Multi-Component Flow with Variable Specific Heat Ratios,” *Journal of Computational Physics*, Vol. 230, No. 23, 2011, pp. 8527–8553.
<https://doi.org/10.1016/j.jcp.2011.07.031>
- [34] Kee, R. J., Miller, J. A., Evans, G. H., and Dixon-Lewis, G., “A Computational Model of the Structure and Extinction of Strained, Opposed Flow, Premixed Methane-Air Flames,” *Symposium (International) on Combustion*, Vol. 22, No. 1, 1989, pp. 1479–1494.
[https://doi.org/10.1016/S0082-0784\(89\)80158-4](https://doi.org/10.1016/S0082-0784(89)80158-4)
- [35] Kee, R. J., Coltrin, M. E., and Glarborg, P., *Chemically Reacting Flow: Theory and Practice*, Wiley, Hoboken, NJ, 2005.
- [36] Goodwin, D. G., Moffat, H. K., and speth, r l, “Cantera: An Object-Oriented Software Toolkit for Chemical Kinetics, Thermodynamics, and Transport Processes,” Ver. 2.4.0, 2018.
<https://doi.org/10.5281/zenodo.1174508>
- [37] Wilke, R., and C, “A Viscosity Equation for Gas Mixtures,” *Journal of Chemical Physics*, Vol. 18, No. 4, 1950, pp. 517–519.
<https://doi.org/10.1063/1.1747673>
- [38] Mathur, S., Tondon, P. K., and Saxena, S. C., “Thermal Conductivity of Binary, Ternary and Quaternary Mixtures of Rare Gases,” *Molecular Physics*, Vol. 12, No. 6, 1967, pp. 569–579.
<https://doi.org/10.1080/00268976700100731>
- [39] Johnson, R. F., and Kercher, A. D., “A Conservative Discontinuous Galerkin Discretization for the Chemically Reacting Navier-Stokes Equations,” *Journal of Computational Physics*, Vol. 423, Dec. 2020, Paper 109826.
<https://doi.org/10.1016/j.jcp.2020.109826>
- [40] Ching, E. J., Johnson, R. F., and Kercher, A. D., “Positivity-Preserving and Entropy-Bounded Discontinuous Galerkin Method for the Chemically Reacting, Compressible Euler Equations. Part I: The One-Dimensional Case,” *Journal of Computational Physics*, Vol. 505, May 2024, Paper 112881.
<https://doi.org/10.1016/j.jcp.2024.112881>
- [41] Hartmann, R., and Houston, P., “An Optimal Order Interior Penalty Discontinuous Galerkin Discretization of the Compressible Navier-Stokes Equations,” *Journal of Computational Physics*, Vol. 227, No. 22, 2008, pp. 9670–9685.
<https://doi.org/10.1016/j.jcp.2008.07.015>
- [42] Ketcheson, D. I., “Highly Efficient Strong Stability-Preserving Runge-Kutta Methods with Low-Storage Implementations,” *Journal on Scientific Computing*, Vol. 30, No. 4, 2008, pp. 2113–2136.
<https://doi.org/10.1137/07070485X>
- [43] Bassi, F., Cecchi, F., Franchina, N., Rebay, S., and Savini, M., “High-Order Discontinuous Galerkin Computation of Axisymmetric Transonic Flows in Safety Relief Valves,” *Computers & Fluids*, Vol. 49, No. 1, 2011, pp. 203–213.
<https://doi.org/10.1016/j.compfluid.2011.05.015>
- [44] DeBoskey, R. D., Kessler, D. A., Bojko, B. T., Johnson, R. F., and Goodwin, G. B., “The Influence of Chemical Reaction Models on Combustion Dynamics in an Opposed-Flow Solid Fuel Burner,” AIAA Paper 2023-0161, Jan. 2023.
<https://doi.org/10.2514/6.2023-0161>
- [45] Arisawa, H., and Brill, T., “Flash Pyrolysis of Hydroxyl-Terminated Polybutadiene (HTPB) II: Implications of the Kinetics to Combustion of Organic Polymers,” *Combustion and Flame*, Vol. 106, Nos. 1–2, 1996, pp. 144–154.
[https://doi.org/10.1016/0010-2180\(95\)00254-5](https://doi.org/10.1016/0010-2180(95)00254-5)
- [46] Kee, R. J., Rupley, F. M., and Miller, J. A., “Chemkin-II: A Fortran Chemical Kinetics Package for the Analysis of Gas-Phase Chemical Kinetics,” SAND TR 89-8009, Sandia National Lab.(SNL-CA), 1989.
- [47] Ciottoli, P. P., Galassi, R. M., Lapenna, P. E., Leccese, G., Bianchi, D., Nasuti, F., Creta, F., and Valorani, M., “CSP-Based Chemical Kinetics Mechanisms Simplification Strategy for Non-Premixed Combustion: An Application to Hybrid Rocket Propulsion,” *Combustion and Flame*, Vol. 186, Dec. 2017, pp. 83–93.
<https://doi.org/10.1016/j.combustflame.2017.07.035>
- [48] Curran, H. J., Gaffuri, P., Pitz, W. J., and Westbrook, C. K., “A Comprehensive Modeling Study of n-Heptane Oxidation,” *Combustion and Flame*, Vol. 114, Nos. 1–2, 1998, pp. 149–177.
[https://doi.org/10.1016/S0010-2180\(97\)00282-4](https://doi.org/10.1016/S0010-2180(97)00282-4)
- [49] Westbrook, C. K., and Dryer, F. L., “Chemical Kinetic Modeling of Hydrocarbon Combustion,” *Progress in Energy and Combustion Science*, Vol. 10, No. 1, 1984, pp. 1–57.
[https://doi.org/10.1016/0360-1285\(84\)90118-7](https://doi.org/10.1016/0360-1285(84)90118-7)
- [50] Andersen, J., Rasmussen, C. L., Giselsson, T., and Glarborg, P., “Global Combustion Mechanisms for Use in CFD Modeling Under Oxy-Fuel Conditions,” *Energy and Fuels*, Vol. 23, No. 3, 2009, pp. 1379–1389.
<https://doi.org/10.1021/ef8003619>
- [51] Olsson, J. O., and Andersson, L. L., “Sensitivity Analysis Based on an Efficient Brute-Force Method, Applied to an Experimental CH₄/O₂ Premixed Laminar Flame,” *Combustion and Flame*, Vol. 67, No. 2, 1987, pp. 99–109.
[https://doi.org/10.1016/0010-2180\(87\)90143-X](https://doi.org/10.1016/0010-2180(87)90143-X)
- [52] Geipel, C. M., Bojko, B. T., Pfützner, C. J., Fisher, B. T., and Johnson, R. F., “Regression of Solid Polymer Fuel Strands in Opposed-Flow Combustion with Gaseous Oxidizer,” *Proceedings of the Combustion Institute*, Vol. 39, No. 3, 2023, pp. 3389–3399.
<https://doi.org/10.1016/j.proci.2022.07.124>
- [53] Vancoillie, J., Demuynck, J., Galle, J., Verhelst, S., and Oijen, J. A. V., “A Laminar Burning Velocity and Flame Thickness Correlation for Ethanol-Air Mixtures Valid at Spark-Ignition Engine Conditions,” *Fuel*, Vol. 102, Dec. 2012, pp. 460–469.
<https://doi.org/10.1016/j.fuel.2012.05.022>
- [54] Veraar, R. G., and Wieling, W. P., “Sustained Combustion Limits of a Central Dump Solid Fuel Ramjet Combustor at High Altitude Operational Conditions,” AIAA Paper 2018-4449, July 2018.
<https://doi.org/10.2514/6.2018-4449>
- [55] Melius, C., Bergan, N., and Shepherd, J., “Effects of Water on Combustion Kinetics at High Pressure,” *Symposium (International) on Combustion*, Vol. 23, 1991, pp. 217–223.
[https://doi.org/10.1016/S0082-0784\(06\)80262-6](https://doi.org/10.1016/S0082-0784(06)80262-6)
- [56] White, F. M., *Fluid Mechanics*, 6th ed., McGraw-Hill Series in Mechanical Engineering, McGraw-Hill, New York, 2009.

Z. Ren
Associate Editor